

Increased atmospheric river frequency slowed the seasonal recovery of Arctic sea ice in recent decades

Pengfei Zhang¹, Chen Gang², Mingfang Ting³, L Ruby Leung⁴, Bin Guan⁵, and Laifang Li¹

¹The Pennsylvania State University

²University of California

³Columbia University

⁴Pacific Northwest National Laboratory

⁵Jet Propulsion Laboratory

November 23, 2022

Abstract

In recent decades, Arctic sea ice coverage experienced a drastic decline in winter, when sea ice is expected to recover following the melting season. Using observations and climate model simulations, we found a robust frequency increase in atmospheric rivers (ARs, intense corridors of moisture transport) over Barents-Kara Seas and the neighboring central Arctic (ABK) in early winter. The extensive moisture carried by more frequent ARs has intensified surface downward longwave radiation and liquid rainfall, caused stronger melting of thin, fragile ice cover, and slowed the seasonal recovery of sea ice, contributing to the sea ice cover decline in ABK. A series of model ensemble experiments suggests that, in addition to a uniform AR increase in response to anthropogenic forcing, the contribution of tropical Pacific variability is indispensable in the observed Arctic AR changes. These findings have significant implications for understanding the rapidly changing Arctic hydroclimate and the cryosphere.

1 Increased atmospheric river frequency slowed the
2 seasonal recovery of Arctic sea ice in recent decades

3
4 Pengfei Zhang^{1*}, Gang Chen², Mingfang Ting³, L. Ruby Leung⁴, Bin Guan^{5,6}, Laifang Li¹
5

6
7 ¹ Department of Meteorology and Atmospheric Science, The Pennsylvania State University,
8 University Park, PA, USA

9 ² Department of Atmospheric and Oceanic Sciences, University of California, Los Angeles, CA,
10 USA

11 ³ Lamont-Doherty Earth Observatory, Columbia University, Palisades, NY, USA

12 ⁴ Atmospheric Sciences and Global Change Division, Pacific Northwest National Laboratory,
13 Richland, WA, USA

14 ⁵ Joint Institute for Regional Earth System Science and Engineering, University of California, Los
15 Angeles, CA, USA

16 ⁶ Jet Propulsion Laboratory, California Institute of Technology, Pasadena, CA, USA
17

18
19
20
21
22
23
24
25
26
27 Initial submission, Feb. 21, 2022

28 Revision, July.30, 2022
29

30
31 * Corresponding author: Pengfei Zhang (pfz5053@psu.edu, zpengfei1006@gmail.com)
32

33 Abstract

34 In recent decades, Arctic sea ice coverage experienced a drastic decline in winter, when sea ice is
35 expected to recover following the melting season. Using observations and climate model
36 simulations, we found a robust frequency increase in atmospheric rivers (ARs, intense corridors
37 of moisture transport) over Barents-Kara Seas and the neighboring central Arctic (ABK) in early
38 winter. The extensive moisture carried by more frequent ARs has intensified surface downward
39 longwave radiation and liquid rainfall, caused stronger melting of thin, fragile ice cover, and
40 slowed the seasonal recovery of sea ice, contributing to the sea ice cover decline in ABK. A series
41 of model ensemble experiments suggests that, in addition to a uniform AR increase in response to
42 anthropogenic forcing, the contribution of tropical Pacific variability is indispensable in the
43 observed Arctic AR changes. These findings have significant implications for understanding the
44 rapidly changing Arctic hydroclimate and the cryosphere.

45

46 Recent decades have witnessed a rapid decline in Arctic sea ice during its winter ice-growing
47 season¹, which raised concerns as Arctic sea ice changes may fuel severe winter storms in mid-
48 latitude continents^{2,3} and reshape the ecosystem and fisheries in the Arctic region^{4,5}. Wintertime
49 sea ice area (SIA) decline, especially in Barents-Kara Seas, has been attributed to atmospheric heat
50 transport by poleward moisture fluxes^{e.g., 6-8}, while enhanced oceanic heat transport through Nordic
51 Sea has aggravated ice thinning and ice volume decline⁹⁻¹⁴.

52

53 The bulk of Arctic moisture import is driven by atmospheric rivers (ARs)¹⁵. ARs are long, narrow,
54 and transient corridors of strong horizontal moisture transport, typically accompanied by a low-
55 level jet ahead of the cold front of an extratropical cyclone¹⁶. Despite covering only 10% of the
56 Earth's circumference in midlatitudes, ARs account for up to 90% of the poleward water vapor
57 transport in these latitudes^{17,18}, playing a crucial role in the hydrological cycle^{e.g., 15, 19-21}. Recent
58 studies reported that ARs can extend into the Arctic circle²². Thus, there is an emergent need to
59 quantify the role of ARs in the recent Arctic climate change.

60

61 In polar regions, contrary to AR-induced snow accumulation in East Antarctica²³, the intense
62 moisture and heat rapidly transported by ARs can exert a strong melting effect on the cryosphere,
63 exemplified by ice sheet melt in Greenland²⁴ and West Antarctica²⁵, polynyas in the Weddell Sea²⁶,
64 and the 2016-17 record low Arctic winter sea ice growth²². The physical processes relevant to AR-
65 induced ice melt or impeded ice growth include (a) enhanced downward longwave radiation (DLW)
66 due to extensive greenhouse effect of atmospheric water vapor, cloud radiative effect, and
67 condensational heating release, (b) reduction or even sign change in turbulent heat fluxes from the
68 ice surface, (c) insulating capacity of snow, and (d) melt energy carried by rainfall^{e.g., 22, 25-31}.

69

70 In recent decades, more frequent ARs have been observed in Greenland and West Antarctica^{24,25},
71 which coincides with the poleward shift of ARs in a warming climate³²⁻³⁴. Our current knowledge
72 of ARs' melting effect leads us to hypothesize that the Arctic AR increase (if it exists over the ice
73 cover) contributes to winter sea ice decline. Although previous works have reported some AR-like
74 plumes, such as moisture intrusions, can induce cold season sea ice loss^{7,35}, these synoptic systems
75 only account for a small fraction (36-38%)⁷ of Arctic moisture import compared to ARs (70-80%)¹⁵
76 (see details in Supplementary Information, SI), and thus are less conclusive of the role of moisture
77 transport in sea ice change. Furthermore, it is not completely understood to what extent human
78 activities have contributed to the high-latitude AR changes in recent decades, affecting mitigation
79 and adaptation planning of the rapidly changing Arctic water cycle.

80

81 This study builds on the established linkage between ARs and surface melting to examine the
82 Arctic AR changes and their role in slowing down the winter Arctic sea ice recovery. We utilize a
83 novel approach with a state-of-the-art climate model to quantify the contributions of anthropogenic
84 forcing and the observed sea surface temperature (SST) variability over the tropical Pacific to
85 Arctic AR changes. We also clarify the mechanisms behind the Arctic AR changes by separating

86 the dynamic (circulation change) and thermodynamic (moistening trend) effects. By focusing on
87 ARs, we connect Arctic sea ice changes with phenomenologically understood extreme weather
88 events (ARs) that account for a large portion of the Arctic moisture import.

89 **ARs' melting effect on Arctic sea ice**

90 The melting effect of Arctic ARs during the ice recovery season (Nov-Dec-Jan, NDJ) in 1979-
91 2021 (Method) is shown in Fig.1. The negative SIC anomalies associated with AR occurrences
92 indicate that ARs significantly retard ice growth throughout all marginal seas, including the
93 Barents-Kara Seas, Hudson Bay, the Labrador Sea, the Baffin Bay, and the Chukchi-Bering Seas
94 (Fig.1a). In the Atlantic sector where the newly formed ice cover is thin^{9,10}, more than half of the
95 sea ice melting occurs during the AR "landfall" over the ice cover (Fig.1b), resulting in a reduction
96 of $\sim 5.5 \times 10^4$ km² sea ice area (SIA, Method) in the Barents-Kara Seas and the neighboring central
97 Arctic to the north (ABK hereafter, the box in Fig.1b) within 3-4 days (Fig.1c).

98
99 The melting effect of ARs on sea ice is dominated by extensive DLW (partly contributed by clouds
100 within ARs) from the intense warm water vapor carried by ARs, as well as AR-induced liquid
101 rainfall (Fig.1c). The snowfall associated with ARs could cause an insulating effect at the sea ice
102 surface, which inhibits ice growth over a much longer timescale (throughout the winter) in this
103 region³⁰, while anomalies of surface turbulent fluxes rapidly decay after the AR landfall. In general,
104 the AR occurrence is significantly correlated with negative SIA anomalies around the ABK area
105 during the ice recovery season, which is robust throughout 1979-2021 (bars in Fig.1d).

106 **Increased AR penetration into the Arctic and its impact on sea ice**

107 In the past several decades, the Arctic has seen a significant increase in AR frequency in the early
108 winter over ABK. This AR trend is robust across three observational datasets (Fig.2b, Fig.S1b-c),
109 coinciding with the most pronounced winter sea ice loss in this region^{e.g., 36}. In contrast, fewer ARs
110 penetrate into inland Eurasia (60°-90°E) to the south of ABK.

111
112 Considering the strong melting effect of ARs, it is tempting to ask if the increased AR frequency
113 could have contributed to the sea ice decline in the past several decades. The observed early winter
114 SIC trend during 1979-2021 features a pronounced decline in the marginal seas, including the
115 ABK, the Greenland Sea, the Labrador Sea, and the Chukchi Sea (Fig.S4a), where ARs exert the
116 melting effect (Fig.1). Since the ARs' melting effect on the shrinkage of Arctic sea ice cover is
117 manifested by DLW and liquid rainfall (Fig.1c), we show the trends of cumulated DLW and liquid
118 rainfall associated with ARs in NDJ in Fig.3(a-b). As the frequency of Arctic ARs increases in the
119 ABK region, the cumulated AR DLW is significantly intensified (Fig.3a), which is partly
120 contributed by the enhanced cloud radiative effect (Fig.S5a). The proportional contribution of the
121 cloud radiative effect to the cumulated AR DLW underscores the role of clouds in enhancing the
122 AR-related DLW (Fig.S6).

123

124 The cumulated AR liquid rainfall, especially along the ice edge where the new ice cover forms, is
125 greatly strengthened (Fig.3b), while the AR-induced snowfall changes are relatively small
126 (Fig.S5b). In the marginal ice zone of ABK, the correlation between SIC and rainfall (-0.61) is
127 even higher than that with DLW (-0.47) during ARs, indicating a strong sea ice melting effect due
128 to AR-related liquid rainfall there. We also examine the above physical processes associated with
129 ARs' melting effect in the coupled climate model experiment of PAC2 (see model experiments in
130 Method, which are analyzed in the next section) in Fig.3(c, d) and Fig.S5(c). The AR-induced
131 DLW and liquid rainfall significantly increase in ABK, consistent with that in observations. Given
132 the above results, it is expected that the increased AR frequency could have enhanced the melting
133 effect of ARs and therefore contributed to the sea ice decline in recent decades.

134
135 To quantify the role of ARs in sea ice change, we examine the SIA growth in ABK, defined as the
136 cumulative sum of the daily anomalies of SIA tendency in NDJ, with and without the contribution
137 from ARs (Method) (Figure 4). Since the Arctic winter surface temperature in the current climate
138 is below the freezing point, it is expected that the general decline of sea ice in summer could lead
139 to a faster thermodynamic ice growth in winter. At the same time, the ice thickness has thinned
140 due to oceanic warming¹¹⁻¹⁴, and thinner ice grows faster^{9,10}. Indeed, a significantly faster SIA
141 growth in NDJ is seen without the ARs' impact (blue line in Fig.4). Along with AR frequency
142 increase, the melting effect on thin, fragile ice cover is enhanced (red line in Fig.4), which partly
143 offsets the fast thermodynamic SIA growth and results in a weak, insignificant positive trend in
144 total SIA growth (black line in Fig.4). Thus, frequent ARs can prevent the sea ice from growing
145 to the extent allowed by the freezing winter surface temperature. Based on the AR's melting effect
146 on ABK SIA as shown by the red line in Fig.4, we calculate the ABK SIA reduction associated
147 with 1% AR frequency, which on average is $-8.8(\pm 0.6) \times 10^4$ km² in NDJ (Method). Then, by
148 projecting the SIA reduction corresponding to 1% AR frequency to the actual AR frequency trend,
149 we estimate the enhancement of the melting effect due to AR frequency increase, which accounts
150 for $\sim 34(\pm 2)\%$ of the total SIA decline in NDJ (Fig.2b). Qualitatively similar results are found in
151 the PAC2 simulations (dashed lines in Fig.4). The SIA growth with and without ARs clearly
152 demonstrates that more frequent ARs slow the seasonal sea ice growth and therefore contribute to
153 the SIA decline during the ice growing season.

154 **Drivers of Arctic AR frequency trends**

155 In order to examine the causes for the Arctic AR trends, we first analyze the Global Ocean Global
156 Atmosphere (GOGA2) experiment, an atmosphere-only model ensemble using CAM6/CESM2
157 forced by historical SST/sea ice and radiative forcing, which includes both the anthropogenic
158 forcing and observed natural variability. Despite the bias of excessive ARs in the Bering Sea, the
159 increasing ARs in the ABK, the AR climatology and the land-sea contrast of the AR changes in
160 the Eurasian sector, are well reproduced in GOGA2 (Fig.5a), suggesting that the model is capable
161 of simulating the observed AR changes.

162

163 To identify the contribution of anthropogenic warming, we analyze the CESM2 Large Ensemble
164 (LENS2), a coupled ocean-atmosphere-sea ice model forced by historical radiative forcing
165 (Methods). The LENS2 ensemble mean, which corresponds to the model response to external
166 radiative forcing, shows a uniform positive trend in AR frequency over the entire high latitudes
167 (Fig.5b). The maximum AR increase in LENS2 is in inland Eurasia, in contrast to fewer ARs in
168 observations and GOGA2 for this region (Fig.2a, Fig.5a-b). Note that LENS2 and GOGA2 use the
169 same atmosphere model and radiative forcing, except that GOGA2 is forced by observed
170 variability in SSTs while LENS2 has internally generated SST variations with suppressed internal
171 variability in its ensemble mean. The distinct spatial patterns of AR trends between LENS2 and
172 GOGA2 suggest a possible role of the different SST variations. Notably, although the model SST
173 biases might contribute to the disagreement between the LENS2 ensemble mean and the observed
174 or GOGA2 AR trends, some LENS2 members share high similarity with GOGA2 and are distinct
175 from the ensemble mean (left column in Fig.S8), further supporting a possible role of internal
176 variability in the modeled and observed AR trends.

177
178 To examine the role of the observed SST variability, we employ a “pacemaker” experiment (PAC2)
179 same as LENS2, except that the tropical Pacific SSTa is nudged towards the observed variations
180 (Methods). We focus on the tropical Pacific here as it is the region with the most prominent modes
181 of natural climate variability, that can exert a stronger influence on the Arctic than any other ocean
182 basins^{37,38}. Figure 5(c) shows that PAC2 captures the significant AR increases around the ABK
183 region with a spatial pattern similar to that of GOGA2. By comparing the spatial patterns of AR
184 trends in PAC2 and LENS2, with the tropical Pacific SST variability being the only difference
185 between the two, it can be inferred that the tropical Pacific influence is non-negligible and must
186 be considered to fully understand the observed AR trends in the Arctic.

187
188 The PAC2 results are designed to represent the combined effects of anthropogenic warming and,
189 at least partly, the observed tropical Pacific influence. Since these two factors are largely additive,
190 the contribution of tropical Pacific variability can be obtained by calculating the differences
191 between PAC2 and LENS2, as shown in Fig.5(d) (see Method for more detailed interpretation and
192 caveats). The observed variability from the tropical Pacific increases the AR frequency in the
193 eastern Arctic, especially north of the ABK region, while significantly fewer ARs are found in
194 inland Eurasia (Fig.5d). These results suggest that tropical Pacific variability is indispensable to
195 simulate the observed spatial pattern of AR changes in the Arctic and Eurasian high latitudes.

196
197 To further quantify the AR trends in ABK and the relative contributions of anthropogenic warming
198 versus tropical Pacific influence, Fig.5(e) shows the uncertainties of the area-averaged AR trends
199 for ABK in the three sets of model experiments. The 95% confidence interval of GOGA2
200 encompasses the observed trend, indicating that the model forced with anthropogenic forcing and
201 historical SST can capture the observed AR trend. In contrast, the observed AR trend is outside
202 the 95% confidence intervals of the anthropogenic change alone (LENS2) or the tropical Pacific

203 influence alone (PAC2-LENS2). This suggests that the observed AR change cannot be fully
204 explained by either external forcing or tropical Pacific variability alone, but rather the combined
205 effect of anthropogenic forcing and internal climate variability. Based on Fig. 5e, the tropical
206 Pacific influence accounts for $38(\pm 12)\%$ of the AR changes in PAC2. Note that the fraction will
207 depend on the model's equilibrium climate sensitivity, which at 5.3K in CESM2 is larger than the
208 best estimated range of 1.5-4.5K³⁹. It implies that the contribution of tropical Pacific SST
209 variability could be even higher in reality.

210 **Mechanisms for Arctic AR changes**

211 We further examine the mechanisms of the AR trends over the high latitudes in 0° - $110^{\circ}E$ in the
212 past few decades. Since water vapor transport is the product of wind and moisture content, the
213 mechanisms for the AR changes in a warming climate can be roughly divided into the part due to
214 trends in wind (dynamic effect) and atmospheric moisture content (thermodynamic effect,
215 consistent with Clausius-Clapeyron relation)^{e.g., 34}. The decomposition of the two parts (See
216 Methods for details) is shown in Fig.6. In observations, the AR increase in ABK is dominated by
217 the thermodynamic effect, while the fewer ARs in west Eurasia are explained by the dynamic
218 effect (Fig.6a-c). The thermodynamic AR increases in the Arctic are consistent with the increase
219 in the atmosphere's water holding capacity due to fast Arctic warming, which supports increased
220 AR frequency observed in the Arctic in recent decades. This is distinct from the high latitude AR
221 increases observed in the Southern Hemisphere, which is dominated by the poleward shifted
222 midlatitude jet, thus a dynamic effect³³. The dynamical AR decrease in west Eurasia may be related
223 to more persistent Ural blocking in recent decades⁴⁰, which suppresses cyclonic AR circulation.
224 These land-sea contrasts in AR changes can also be seen in GOGA2 and PAC2, both, at least partly,
225 constrained by the observed tropical Pacific variability (Fig.6 d-f, j-l). In fact, the tropical Pacific
226 SSTa nudged to observations in the otherwise free running PAC2 experiment can produce a
227 tropical Pacific-Arctic teleconnection, contributing to a warm Arctic^{37,41}. This warming induced by
228 tropical Pacific variability in combination with anthropogenic forcing favors more frequent ARs
229 in the Arctic, which is well captured by GOGA2 and PAC2 (Fig.6 f, l).

230
231 In contrast, there is a weak dynamical contribution and a strong thermodynamic increase in inland
232 west Eurasia in the ensemble mean of LENS2 (Fig.6 h, i), leading to the maximum AR increase
233 over west Eurasia (Fig.6g and Fig.5b). These differences between the LENS2 ensemble mean and
234 observation in the spatial distributions of dynamic and thermodynamic effects can be attributed to
235 the suppressed natural variability. Several ensemble members of LENS2, however, capture the
236 maximum thermodynamic effect in the Arctic as in GOGA2 and PAC2 (Fig.S8), further suggesting
237 the considerable role of internal variability in the simulated Arctic AR increases.

238 **Summary**

239 In this study, we show a robust frequency increase in ARs that penetrate into the Arctic in the ice
240 growing season in recent decades, especially over the ABK region. ARs, which dominate the

241 Arctic moisture import, induce a strong melting effect, especially on the newly-formed thin and
242 fragile sea ice, through enhanced downward longwave radiation from the AR-transported water
243 vapor and heat and the associated liquid rainfall. Given the thinner ice cover aggravated by warmer
244 ocean water mass^{e.g., 9,11–14}, more frequent ARs result in a stronger melting effect on sea ice in the
245 winter ice growing season, slowing down the seasonal sea ice recovery in recent decades and
246 accounting for 34(±2)% of the observed sea ice area decline in early winter ABK. Using state-of-
247 the-art model ensembles and a novel pacemaker approach, we further demonstrate that, in addition
248 to a uniform AR increase in response to anthropogenic forcing, the observed tropical Pacific SST
249 variability is indispensable in producing the observed AR changes around the Arctic in the past
250 few decades. The increased frequency in Arctic ARs, in turn, is mainly due to the warming-driven
251 moistening.

252
253 The AR frequency increase manifests the intensifying hydrological cycle in the Arctic^{42–44}, and
254 could exert impacts beyond hydrology and the cryosphere in the Arctic. Combined with more
255 frequent cyclones in the central Arctic and Chukchi Sea^{45–47}, the resultant rainfall and snowfall are
256 expected to experience pronounced changes^{48,49}, leading to a more stormy Arctic. These changes
257 will increase the ecosystem fragility and human exposure to natural hazards in the Arctic as
258 international ocean freight and fishing industries are expected to grow there in the coming decades.
259 Advancing our understanding of the changes in the synoptic weather systems such as ARs in a
260 warming climate could lead to more credible projections of ecosystem changes and human
261 adaptation to the growing impacts of global warming in the polar region.

262

263 **Methods**

264 **Observational datasets**

265 Three reanalysis datasets are employed in this study: the European Centre for Medium-Range
266 Weather Forecasts (ECMWF) 5th generation reanalysis (ERA5)⁵⁰ in 1979–2021 at a resolution of
267 $0.5^\circ \times 0.5^\circ$, National Aeronautics and Space Administration (NASA) Modern-Era Retrospective
268 analysis for Research and Applications, version 2 (MERRA2)⁵¹ in 1980–2021 at $0.625^\circ \times 0.5^\circ$, and
269 Japan Meteorological Agency Japanese 55-year Reanalysis (JRA55)⁵² in 1979–2021 at $1.5^\circ \times 1.5^\circ$.
270 We focus on the long-term changes in the sea ice seasonal recovery months November–December–
271 January (NDJ), and thus there are 42 NDJ in ERA5 and JRA55, and 41 NDJ in MERRA2 analyzed.
272 Daily variables are used, but the results are robust using 6-hourly data (See Fig.S1a vs Fig.2a). See
273 Supplementary Information (SI) for the quality and validation of reanalysis data.

274

275 The sea ice data is NOAA/National Snow and Ice Data Center (NSIDC) climate data record of
276 satellite passive microwave sea ice concentration (SIC), version 4⁵³. Both daily and monthly SIC
277 estimates during 1979–2021 from the NASA Bootstrap algorithm on a $25\text{km} \times 25\text{km}$ grid are used.
278 Note that satellite observation is missing during the 1987–88 winter. The sea ice cover edge is
279 defined as the 15% contour of SIC by convention. Sea ice coverage can be measured in terms of

280 both area and extent (see NSIDC terminology:
 281 <https://nsidc.org/cryosphere/seaice/data/terminology.html>). Sea ice extent (SIE) measures the
 282 ocean region surrounded by sea ice cover edge line. Sea ice area (SIA) at each grid cell is calculated
 283 as SIC multiplying the cell area, i.e., the area of the portion of the cell covered by ice. For example,
 284 for a grid cell with SIC of 50%, the whole grid cell is treated as ice covered (SIC>15%) in
 285 determining SIE, while only 50% of the grid cell is counted in SIA. There is almost no difference
 286 between SIE and SIA from the view of long-term change and large scale. We use SIA in this study
 287 because SIA represents the exact variations of sea ice coverage and thus is appropriate to reflect
 288 the ARs' impact at the synoptic temporal and spatial scales. The NDJ SIA growth in Fig.4 is
 289 defined as the cumulative sum of daily anomalies of SIA tendency in NDJ. The SIA tendency on
 290 the i day is defined as $(SIA_{i+1}-SIA_{i-1})/2$, where i denotes the day number during Nov.1-Jan.31. The
 291 daily anomaly is the deviation from the daily mean of the whole study period of each dataset
 292 smoothed with a 15-day moving average window. SIA growth associated with (without) AR is the
 293 cumulated sum of SIA tendency with (without) AR occurrence. We focus on ice coverage because
 294 of the distinct surface energy balance and air-sea interaction with and without ice cover on the sea
 295 surface.

296

297 **Model experiments and interpretation**

298 This study involves a series of model ensemble experiments conducted by Climate Variability and
 299 Change Working Group (CVCWG, https://www.cesm.ucar.edu/working_groups/CVC/) at
 300 National Center for Atmospheric Research (NCAR) using the state-of-the-art global climate model
 301 CESM2. First, the 50-member CESM2 Large Ensemble (LENS2)⁵⁴ outputs are employed. LENS2
 302 covers the period 1850-2100 under CMIP6 historical (before 2014) and SSP370 (from 2015) future
 303 radiative forcing scenarios. Each ensemble member is forced in an identical way, except for the
 304 initial conditions. The LENS2 ensemble can be regarded as an expansion set of the CESM2
 305 simulations in the CMIP6 archive. The results in LENS2 are therefore generally similar to the
 306 CESM2 simulations in CMIP6, which we have confirmed. Second, we examine a 10-member
 307 atmosphere-only simulation from CAM6, the atmospheric component of CESM2, forced by the
 308 same external forcing as LENS2 and prescribed time-varying SST from NOAA Extended
 309 Reconstruction Sea Surface Temperature Version 5 (ERSSTv5) and Hadley Centre sea ice
 310 (HadISST1) from 1880-2019, named as Global Ocean Global Atmosphere. This set of simulations
 311 is called GOGA2 to differentiate it from a similar set of simulations produced by CAM5/CESM1.
 312 Third, we analyze a 10-member pacemaker historical experiment with CESM2 in which the time-
 313 evolving SST anomalies (SSTa) in the tropical Pacific are nudged to observations (ERSSTv5).
 314 The nudging mask covers the tropical Pacific from the American coast to the western Pacific
 315 between 20°S-20°N, with the form of a wedge shape toward the Maritime Continent to the west
 316 of the dateline, and a 5-degree buffer region where the strength of the relaxation is linearly reduced.
 317 In each pacemaker run, the model simulated temporal SSTa is replaced with the observed evolution
 318 of SSTa (i.e., the tropical Pacific SSTa is the pacemaker), with the rest of the model's coupled
 319 climate system free to evolve. Since only the anomalies are nudged, the nudging does not alter the

320 mean state of the model. In the period of 1980s-2010s, there is a decadal cooling trend in the
321 tropical Pacific (i.e., a La-Nina-like change), known as the phase transition of Inter-decadal Pacific
322 Oscillation (IPO) or Pacific Decadal Oscillation (PDO), the leading mode of internal variability at
323 the decadal timescale featuring SST variability in the Pacific Ocean. See the webpage
324 (https://www.cesm.ucar.edu/working_groups/CVC/simulations/cesm2-pacific_pacemaker.html)
325 for the nudging mask area and the details of the Pacific Pacemaker experiments. This CESM2
326 Pacific Pacemaker ensemble is called PAC2 in this study.

327

328 The daily and monthly outputs are available at the same resolution of $0.9^{\circ} \times 1.25^{\circ}$. We only
329 analyzed the outputs in 1979-2014 in which all experiments are forced by the historical forcing to
330 facilitate a comparison to the observations, i.e., 35 NDJ in each member for analysis.

331

332 As the three experiments (GOGA2, LENS2, and PAC2) share the same radiative forcing and use
333 the same atmospheric model, the differences among them lie in the surface boundary conditions
334 for the atmosphere: prescribed observed SST (GOGA2), coupled ocean-atmosphere except for the
335 tropical Pacific SST which is constrained by the observed IPO evolution (PAC2), and fully coupled
336 ocean-atmosphere (LENS2). With these experimental setups, the climate evolution in GOGA2 is
337 most comparable to observations, followed by PAC2, while LENS2 is free to evolve subject only
338 to external forcing.

339

340 We interpret the model results following the well established approach in the climate modeling
341 community^{e.g., 55-57}. The observed climate reflects the combination of the radiatively forced
342 response and a specific realization of the natural variability. Because the latter is random, we would
343 not expect an individual member of the free running model ensembles to closely resemble the
344 observation. Although free running models cannot perfectly reproduce the exact phase of the
345 observed natural variability, model ensembles can be used to separate the influences of external
346 forcing and internal variability. The influence of anthropogenic forcing, i.e., the forced response,
347 can be estimated by the ensemble mean of LENS2, because each member of the ensemble is
348 influenced by the same external forcing while the internal variability is largely suppressed by
349 averaging across the individual ensemble members which feature different realizations of the
350 random natural variability. In other words, the spread among the ensemble members in LENS2
351 represents the effects of random internal variability. With the tropical Pacific SSTa nudged to the
352 observations, the PAC2 ensemble spread represents internal variability associated with regions
353 outside the tropical Pacific and with internal atmospheric dynamics, while its ensemble mean
354 reflects the combination of the anthropogenically forced responses and the model's responses to
355 the observed tropical Pacific SST variability. Since PAC2 and LENS2 share the same model
356 configurations, their forced responses should in principle be the same, and therefore the forced
357 response in both LENS2 and PAC2 can be represented by the ensemble mean of LENS2. Then,
358 the role of the tropical Pacific SST variability, called "tropical Pacific influence", can be isolated
359 by subtracting the LENS2 ensemble mean from the PAC2 mean⁵⁵⁻⁵⁷. The tropical Pacific influence

360 is an estimate of the variability in the climate system that is associated with tropical Pacific SSTs.
361 Ref⁵⁵ concluded that this approach allows us to consistently compare the magnitude of climate
362 responses (for example, Arctic AR changes) to anthropogenic forcing and tropical Pacific
363 variability. The significant difference between the PAC2 and LENS2 mean AR trends in northern
364 ABK and inland Eurasia (Fig.5d) suggests that the Pacific variability played a detectable role in
365 the high-latitude AR trend during recent decades.

366
367 There are caveats in understanding the influence of tropical Pacific variability based on the model
368 experiments. First, the estimate of the tropical influence assumes that the responses to tropical
369 Pacific variability and external forcings are independent. Indeed, they are largely linearly separable
370 for all practical purposes^{e.g., 58–60}, although this assumption may not strictly hold. In any case, it is
371 difficult to completely separate the external and tropical signals. Thus, the linear assumption in
372 fact neglects the impact of external forcing on tropical Pacific variability⁵⁵. Second, it is possible
373 that the forced response in LENS2 and PAC2 may not be the same. Nevertheless, many previous
374 studies have shown that the above approach practically and realistically delineates the response to
375 tropical Pacific variability^{e.g., 55–57}.

376
377 Third, some biases in model physics may affect sea ice simulation and ARs' impact on sea ice in
378 CESM2. Over the Arctic, the CESM2 configuration has thinner liquid clouds and less cloud
379 fraction due to underestimated aerosols, leading to much more shortwave radiation received by
380 sea ice in melt season and thus an insufficient late summer Arctic sea ice cover, while the sea ice
381 coverage bias is relatively small in winter^{e.g., 61,62}. The sea ice bias could produce a faster ice growth
382 in early winter, debasing the significance of ARs' melting effect on sea ice in CESM2 simulations,
383 as we can see in Fig.4. In addition, less cloud fraction may also reduce the contribution of cloud
384 to DLW. On the other hand, the winter ice thickness in CESM2 is biased thin in historical
385 simulations⁶³, which could enhance the ARs' melting effect. That is to say, biases in CESM2
386 physics may partly cancel each other to simulate the ARs' impact on sea ice, and could explain the
387 weaker melting effect of ARs simulated in PAC2 than observation (Fig.4). Furthermore, given that
388 the Gulf stream warming in CESM2 lies towards the higher end of CMIP6 models⁶⁴, the
389 underestimation of the winter SIC decline in Barents-Kara Seas in recent decades in CESM2 (See⁶⁴
390 or Fig.S4) may be attributable to the underestimation of atmospheric influences such as the weaker
391 ARs' melting effect in CESM2. Nevertheless, given that the ensembles employed in the current
392 study are based on the same model, the model bias may be canceled when one ensemble is
393 subtracted from another and thus may not affect the understanding of the tropical Pacific influence
394 obtained from (PAC2 minus LENS2).

395

396 **AR detection and analysis methods**

397 We employ an IVT-based AR detection algorithm originally developed by ref⁶⁵ and slightly
398 optimize it for the Arctic following ref²⁴. The algorithm by ref⁶⁵ is recommended by the
399 Atmospheric River Tracking Method Intercomparison Project (ARTMIP), especially for research

400 on ARs in polar latitudes and inland regions⁶⁶. ARTMIP noted that this algorithm is one of the
 401 methods that facilitate the attribution of impacts within the AR footprint⁶⁶. In fact, all ARTMIP
 402 global algorithms tend to agree remarkably well on the AR footprints⁶⁷. In the algorithm used in
 403 this study, the monthly dependent 85th percentile of the IVT magnitude at each grid cell, or 100 kg
 404 $\text{m}^{-1} \text{ s}^{-1}$, whichever is greater, is used as the intensity threshold to identify contiguous regions with
 405 elevated IVT. In practice, the 85th percentile IVT is the threshold used in the midlatitudes, same as
 406 many other algorithms⁶⁶, while $100 \text{ kg m}^{-1} \text{ s}^{-1}$ is the actual threshold used in the Arctic region
 407 because of the low IVT due to low air temperature. We also checked the ARs with relative
 408 thresholds in the Arctic and the results are not sensitive to the choice of thresholds (See the
 409 discussion in SI and FigS.1 d-f). Potential ARs are then filtered by applying size, length, length-
 410 to-width ratio, coherence, the meridional component of mean IVT, and mean transport direction
 411 criteria. We follow ref²⁴ to change the length criterion from 2000km to 1500km, considering the
 412 ARs reaching the Arctic are usually at the end of their lifecycle and their size shrinks (In fact, the
 413 results are not sensitive to the change of length criterion, not shown). These requirements ensure
 414 that the identified characteristics are long, narrow, coherent belts of poleward moisture transport
 415 in (and connecting) the midlatitudes and polar regions, i.e., they bear the features of ARs. See
 416 refs^{24,65} for additional details on the AR detection algorithm.

417
 418 A scaling method³³ is employed to separate the thermodynamic effect and the dynamical effect in
 419 the AR frequency trend. We create a hypothetical scenario of daily IVT with dynamic effect only
 420 by applying a scaling coefficient to specific humidity, given the moisture changes are expected to
 421 scale in line with the CC relationship. Specifically, the specific humidity is scaled by a factor,
 422 q_c/q_y , where q_c is the climatological specific humidity in NDJ at the level and grid to which this
 423 factor applies and q_y is the mean specific humidity at the same grid for the given NDJ. By scaling
 424 the data this way, the year-to-year change in specific humidity is removed. Then, the IVT
 425 calculated with the scaled moisture field and the same threshold are used as input to the AR
 426 detection algorithm. As a result, the effect of the background moisture interannual variability on
 427 AR variability is suppressed, allowing the AR trend due to the dynamic effect to be estimated.
 428 Ref⁶⁸ found that the two components are largely linearly additive using the same method.
 429 Therefore, we calculate the thermodynamic effect as the difference between the total trend and the
 430 dynamic effect.

431
 432 Variable (DLW, rainfall, snowfall, SIC, etc.) anomalies associated with ARs at a grid are detected
 433 if an AR appears at this grid. The climatology or reference state refers to the mean of the whole
 434 study period of each dataset smoothed with a 15-day moving average window. For the AR-related
 435 trends in variables (DLW, cloud radiative effect, rainfall, and snowfall) shown in Fig.3, Fig.S2b,
 436 Fig.S5, and Fig.S6, we first integrate the variable associated with ARs in NDJ over time (i.e., the
 437 total/cumulated amount of these fluxes related to ARs) and then calculate the trends. The
 438 contribution of cloud radiative effect to DLW is the difference between surface DLW and clear
 439 sky DLW. The results are qualitatively similar if we take into account the persistence (3-day after

440 landfall even the ARs decay, Fig.1c) of ARs' impact in detecting the AR-related variable
 441 anomalies (not shown). The impact of ice drifting related to AR wind on ABK SIA is much smaller
 442 than that of AR's melting effect (see SI) and thus not be involved in this study.

443
 444 Linear projection is used to determine the amount of enhancement of AR melting effect due to AR
 445 frequency increase. We first calculate the melting effect on SIA corresponding to 1% AR
 446 frequency (~ 0.92 day) occurrence based on the SIA growth with AR (red line in Fig.4) and AR
 447 frequency (Fig.2b) in NDJ, which on average is a reduction of $-8.8(\pm 0.6) \times 10^4$ km² in ABK SIA in
 448 NDJ in the observation. Uncertainty is measured by the standard error computed from interannual
 449 time series. Then we can estimate the enhancement of the melting effect due to AR frequency
 450 increase by projecting the SIA reduction corresponding to 1% AR frequency to the actually trend
 451 in AR frequency (Fig.2b), and finally infer its contribution ($\sim 34\% \pm 2\%$) to the SIA decline in ABK
 452 in NDJ (red line in Fig.2b). The contribution is $30(\pm 5)\%$ in PAC2 due to a weaker melting effect
 453 simulated in CESM2. The uncertainty in PAC2 is the standard error cross ensemble members.

454 455 **Statistics methods**

456 The Student *t*-test is used in the significance test for the linear trend in observations. A 1000-trail
 457 bootstrap resampling with replacement is used in the significance tests for the composite analysis
 458 and the trends in model ensembles. Following Ref⁶⁹, the uncertainty in the mean trend of an
 459 ensemble is represented by the 95% confidence interval, which is given by $\bar{b} \pm \frac{c s_b}{\sqrt{n}}$, where \bar{b} is the
 460 ensemble mean of the trends calculated from individual ensemble members, n is the ensemble size,
 461 c is the 97.5th percentile of the Student's *t* distribution with $n-1$ degrees of freedom, s_b is an
 462 estimate of the inter-member variance of the trends. We calculate this 95% confidence interval for
 463 GOGA2, LENS2, and PAC2, shown as the vertical color bars in Fig.5e. The pattern correlation
 464 coefficient (PCC) is employed to measure the pattern similarity between the individual run of
 465 LENS2 and the ensemble mean of GOGA2 (PAC2) with latitudinal weights considered.

466 467 **Data availability**

468 The data acquisition information for the simulations used in this study can be found on
 469 CVCWG/NCAR webpage (https://www.cesm.ucar.edu/working_groups/CVC/). ERA5,
 470 MERRA2, and JRA55 reanalysis data are available from
 471 <https://cds.climate.copernicus.eu/#!/home>, [https://gmao.gsfc.nasa.gov/reanalysis/MERRA-](https://gmao.gsfc.nasa.gov/reanalysis/MERRA-2/data_access/)
 472 [2/data_access/](https://gmao.gsfc.nasa.gov/reanalysis/MERRA-2/data_access/), and https://jra.kishou.go.jp/JRA-55/index_en.html. NSIDC sea ice concentration
 473 is available from <https://nsidc.org/data/G02202>. See SI for the download information of the data
 474 used in SI.

475 476 **Code availability**

477 The code of the AR detection method used in this study can be downloaded at:
 478 <https://doi.org/10.25346/S6/SJGRKY>. Other analysis codes are available from the corresponding
 479 author upon request.

480 **References**

- 481 1. Stroeve, J. C. *et al.* Trends in Arctic sea ice extent from CMIP5, CMIP3 and observations.
482 *Geophys. Res. Lett.* **39**, L16502 (2012).
- 483 2. Bailey, H. *et al.* Arctic sea-ice loss fuels extreme European snowfall. *Nature Geoscience* 1–6
484 (2021) doi:10.1038/s41561-021-00719-y.
- 485 3. Cohen, J., Agel, L., Barlow, M., Garfinkel, C. I. & White, I. Linking Arctic variability and
486 change with extreme winter weather in the United States. *Science* (2021)
487 doi:10.1126/science.abi9167.
- 488 4. Dalpadado, P. *et al.* Productivity in the Barents Sea - Response to Recent Climate
489 Variability. *PLOS ONE* **9**, e95273 (2014).
- 490 5. Fossheim, M. *et al.* Recent warming leads to a rapid borealization of fish communities in the
491 Arctic. *Nature Clim Change* **5**, 673–677 (2015).
- 492 6. Park, D.-S. R., Lee, S. & Feldstein, S. B. Attribution of the Recent Winter Sea Ice Decline
493 over the Atlantic Sector of the Arctic Ocean. *J. Clim.* **28**, 4027–4033 (2015).
- 494 7. Woods, C. & Caballero, R. The Role of Moist Intrusions in Winter Arctic Warming and Sea
495 Ice Decline. *Journal of Climate* **29**, 4473–4485 (2016).
- 496 8. Hofsteenge, M. G., Graversen, R. G., Rydsaa, J. H. & Rey, Z. The impact of atmospheric
497 Rossby waves and cyclones on the Arctic sea ice variability. *Clim Dyn* (2022)
498 doi:10.1007/s00382-022-06145-z.
- 499 9. Petty, A. A., Holland, M. M., Bailey, D. A. & Kurtz, N. T. Warm Arctic, Increased Winter
500 Sea Ice Growth? *Geophysical Research Letters* **45**, 12,922–12,930 (2018).
- 501 10. Stroeve, J. & Notz, D. Changing state of Arctic sea ice across all seasons. *Environ. Res. Lett.*
502 **13**, 103001 (2018).
- 503 11. Barton, B. I., Lenn, Y.-D. & Lique, C. Observed Atlantification of the Barents Sea Causes
504 the Polar Front to Limit the Expansion of Winter Sea Ice. *Journal of Physical Oceanography*
505 **48**, 1849–1866 (2018).
- 506 12. Polyakov, I. V. *et al.* Borealization of the Arctic Ocean in Response to Anomalous
507 Advection From Sub-Arctic Seas. *Frontiers in Marine Science* **7**, (2020).
- 508 13. Skagseth, Ø. *et al.* Reduced efficiency of the Barents Sea cooling machine. *Nature Climate*
509 *Change* **10**, 661–666 (2020).
- 510 14. Tsubouchi, T. *et al.* Increased ocean heat transport into the Nordic Seas and Arctic Ocean
511 over the period 1993–2016. *Nat. Clim. Chang.* **11**, 21–26 (2021).
- 512 15. Nash, D., Waliser, D., Guan, B., Ye, H. & Ralph, F. M. The Role of Atmospheric Rivers in
513 Extratropical and Polar Hydroclimate. *Journal of Geophysical Research: Atmospheres* **123**,
514 6804–6821 (2018).
- 515 16. Ralph, F. M. *et al.* Atmospheric Rivers Emerge as a Global Science and Applications Focus.
516 *Bulletin of the American Meteorological Society* **98**, 1969–1973 (2017).
- 517 17. Zhu, Y. & Newell, R. E. A Proposed Algorithm for Moisture Fluxes from Atmospheric
518 Rivers. *Monthly Weather Review* **126**, 725–735 (1998).

- 519 18. Newman, M., Kiladis, G. N., Weickmann, K. M., Ralph, F. M. & Sardeshmukh, P. D.
520 Relative Contributions of Synoptic and Low-Frequency Eddies to Time-Mean Atmospheric
521 Moisture Transport, Including the Role of Atmospheric Rivers. *J. Climate* **25**, 7341–7361
522 (2012).
- 523 19. Lavers, D. A. & Villarini, G. The contribution of atmospheric rivers to precipitation in
524 Europe and the United States. *Journal of Hydrology* **522**, 382–390 (2015).
- 525 20. Chen, X., Leung, L. R., Wigmosta, M. & Richmond, M. Impact of Atmospheric Rivers on
526 Surface Hydrological Processes in Western U.S. Watersheds. *Journal of Geophysical*
527 *Research: Atmospheres* **124**, 8896–8916 (2019).
- 528 21. Skinner, C. B., Lora, J. M., Payne, A. E. & Poulsen, C. J. Atmospheric river changes shaped
529 mid-latitude hydroclimate since the mid-Holocene. *Earth and Planetary Science Letters* **541**,
530 116293 (2020).
- 531 22. Hegyi, B. M. & Taylor, P. C. The Unprecedented 2016–2017 Arctic Sea Ice Growth Season:
532 The Crucial Role of Atmospheric Rivers and Longwave Fluxes. *Geophysical Research*
533 *Letters* **45**, 5204–5212 (2018).
- 534 23. Gorodetskaya, I. V. *et al.* The role of atmospheric rivers in anomalous snow accumulation in
535 East Antarctica. *Geophysical Research Letters* **41**, 6199–6206 (2014).
- 536 24. Mattingly, K. S., Mote, T. L. & Fettweis, X. Atmospheric River Impacts on Greenland Ice
537 Sheet Surface Mass Balance. *Journal of Geophysical Research: Atmospheres* **123**, 8538–
538 8560 (2018).
- 539 25. Wille, J. D. *et al.* West Antarctic surface melt triggered by atmospheric rivers. *Nature*
540 *Geoscience* **12**, 911–916 (2019).
- 541 26. Francis, D., Mattingly, K. S., Temimi, M., Massom, R. & Heil, P. On the crucial role of
542 atmospheric rivers in the two major Weddell Polynya events in 1973 and 2017 in Antarctica.
543 *Science Advances* **6**, eabc2695 (2020).
- 544 27. Persson, P. O. G., Shupe, M. D., Perovich, D. & Solomon, A. Linking atmospheric synoptic
545 transport, cloud phase, surface energy fluxes, and sea-ice growth: observations of midwinter
546 SHEBA conditions. *Clim Dyn* **49**, 1341–1364 (2017).
- 547 28. Doyle, S. H. *et al.* Amplified melt and flow of the Greenland ice sheet driven by late-summer
548 cyclonic rainfall. *Nature Geosci* **8**, 647–653 (2015).
- 549 29. Ledley, T. S. Snow on sea ice: Competing effects in shaping climate. *Journal of Geophysical*
550 *Research: Atmospheres* **96**, 17195–17208 (1991).
- 551 30. Merkouriadi, I., Cheng, B., Hudson, S. R. & Granskog, M. A. Effect of frequent winter
552 warming events (storms) and snow on sea-ice growth – a case from the Atlantic sector of the
553 Arctic Ocean during the N-ICE2015 campaign. *Annals of Glaciology* **61**, 164–170 (2020).
- 554 31. Wang, Z., Walsh, J., Szymborski, S. & Peng, M. Rapid Arctic Sea Ice Loss on the Synoptic
555 Time Scale and Related Atmospheric Circulation Anomalies. *Journal of Climate* **33**, 1597–
556 1617 (2020).

- 557 32. Gao, Y., Lu, J. & Leung, L. R. Uncertainties in Projecting Future Changes in Atmospheric
558 Rivers and Their Impacts on Heavy Precipitation over Europe. *J. Clim.* **29**, 6711–6726
559 (2016).
- 560 33. Ma, W., Chen, G. & Guan, B. Poleward Shift of Atmospheric Rivers in the Southern
561 Hemisphere in Recent Decades. *Geophysical Research Letters* **47**, e2020GL089934 (2020).
- 562 34. Payne, A. E. *et al.* Responses and impacts of atmospheric rivers to climate change. *Nature*
563 *Reviews Earth & Environment* **1**, 143–157 (2020).
- 564 35. Yang, W. & Magnusdottir, G. Springtime extreme moisture transport into the Arctic and its
565 impact on sea ice concentration. *Journal of Geophysical Research: Atmospheres* **122**, 5316–
566 5329 (2017).
- 567 36. Onarheim, I. H. & Årthun, M. Toward an ice-free Barents Sea. *Geophysical Research Letters*
568 **44**, 8387–8395 (2017).
- 569 37. Meehl, G. A., Chung, C. T. Y., Arblaster, J. M., Holland, M. M. & Bitz, C. M. Tropical
570 Decadal Variability and the Rate of Arctic Sea Ice Decrease. *Geophysical Research Letters*
571 **45**, 11,326–11,333 (2018).
- 572 38. Wu, Y., Lu, J., Ding, Q. & Liu, F. Linear Response Function Reveals the Most Effective
573 Remote Forcing in Causing September Arctic Sea Ice Melting in CESM. *Geophysical*
574 *Research Letters* **48**, e2021GL094189 (2021).
- 575 39. Gettelman, A. *et al.* High Climate Sensitivity in the Community Earth System Model
576 Version 2 (CESM2). *Geophysical Research Letters* **46**, 8329–8337 (2019).
- 577 40. Luo, D. *et al.* Impact of Ural Blocking on Winter Warm Arctic–Cold Eurasian Anomalies.
578 Part I: Blocking-Induced Amplification. *Journal of Climate* **29**, 3925–3947 (2016).
- 579 41. Clark, J. P. & Lee, S. The Role of the Tropically Excited Arctic Warming Mechanism on the
580 Warm Arctic Cold Continent Surface Air Temperature Trend Pattern. *Geophys. Res. Lett.* **0**,
581 (2019).
- 582 42. Vihma, T. *et al.* The atmospheric role in the Arctic water cycle: A review on processes, past
583 and future changes, and their impacts. *Journal of Geophysical Research: Biogeosciences*
584 **121**, 586–620 (2016).
- 585 43. Gimeno, L. *et al.* Atmospheric moisture transport and the decline in Arctic Sea ice. *WIREs*
586 *Climate Change* **10**, e588 (2019).
- 587 44. Bintanja, R. *et al.* Strong future increases in Arctic precipitation variability linked to
588 poleward moisture transport. *Science Advances* **6**, eaax6869 (2020).
- 589 45. Zhang, X., Walsh, J. E., Zhang, J., Bhatt, U. S. & Ikeda, M. Climatology and Interannual
590 Variability of Arctic Cyclone Activity: 1948–2002. *Journal of Climate* **17**, 2300–2317
591 (2004).
- 592 46. Zahn, M., Akperov, M., Rinke, A., Feser, F. & Mokhov, I. I. Trends of Cyclone
593 Characteristics in the Arctic and Their Patterns From Different Reanalysis Data. *Journal of*
594 *Geophysical Research: Atmospheres* **123**, 2737–2751 (2018).

- 595 47. Valkonen, E., Cassano, J. & Cassano, E. Arctic Cyclones and Their Interactions With the
596 Declining Sea Ice: A Recent Climatology. *Journal of Geophysical Research: Atmospheres*
597 **126**, e2020JD034366 (2021).
- 598 48. Webster, M. A., Parker, C., Boisvert, L. & Kwok, R. The role of cyclone activity in snow
599 accumulation on Arctic sea ice. *Nat Commun* **10**, 5285 (2019).
- 600 49. McCrystall, M. R., Stroeve, J., Serreze, M., Forbes, B. C. & Screen, J. A. New climate
601 models reveal faster and larger increases in Arctic precipitation than previously projected.
602 *Nat Commun* **12**, 6765 (2021).
- 603 50. Hersbach, H. *et al.* The ERA5 global reanalysis. *Quarterly Journal of the Royal*
604 *Meteorological Society* **146**, 1999–2049 (2020).
- 605 51. Gelaro, R. *et al.* The Modern-Era Retrospective Analysis for Research and Applications,
606 Version 2 (MERRA-2). *Journal of Climate* **30**, 5419–5454 (2017).
- 607 52. Kobayashi, S. *et al.* The JRA-55 Reanalysis: General Specifications and Basic
608 Characteristics. *Journal of the Meteorological Society of Japan. Ser. II* **93**, 5–48 (2015).
- 609 53. Meier, W. N., Fetterer, F., Windnagel, A. K. & Stewart, J. S. *NOAA/NSIDC Climate Data*
610 *Record of Passive Microwave Sea Ice Concentration, Version 4.*
611 <https://doi.org/10.7265/efmz-2t65> (2021).
- 612 54. Rodgers, K. B. *et al.* Ubiquity of human-induced changes in climate variability. *Earth*
613 *System Dynamics Discussions* 1–22 (2021) doi:10.5194/esd-2021-50.
- 614 55. Holland, P. R., Bracegirdle, T. J., Dutrieux, P., Jenkins, A. & Steig, E. J. West Antarctic ice
615 loss influenced by internal climate variability and anthropogenic forcing. *Nat. Geosci.* **12**,
616 718–724 (2019).
- 617 56. Schneider, D. P. & Deser, C. Tropically driven and externally forced patterns of Antarctic
618 sea ice change: reconciling observed and modeled trends. *Clim Dyn* **50**, 4599–4618 (2018).
- 619 57. Yang, D. *et al.* Role of Tropical Variability in Driving Decadal Shifts in the Southern
620 Hemisphere Summertime Eddy-Driven Jet. *Journal of Climate* **33**, 5445–5463 (2020).
- 621 58. Ting, M., Kushnir, Y., Seager, R. & Li, C. Forced and Internal Twentieth-Century SST
622 Trends in the North Atlantic*. *J. Clim.* **22**, 1469–1481 (2009).
- 623 59. DelSole, T., Tippett, M. K. & Shukla, J. A Significant Component of Unforced Multidecadal
624 Variability in the Recent Acceleration of Global Warming. *Journal of Climate* **24**, 909–926
625 (2011).
- 626 60. Lu, J., Hu, A. & Zeng, Z. On the possible interaction between internal climate variability and
627 forced climate change. *Geophysical Research Letters* **41**, 2962–2970 (2014).
- 628 61. DuVivier, A. K. *et al.* Arctic and Antarctic Sea Ice Mean State in the Community Earth
629 System Model Version 2 and the Influence of Atmospheric Chemistry. *Journal of*
630 *Geophysical Research: Oceans* **125**, e2019JC015934 (2020).
- 631 62. Kay, J. E. *et al.* Less Surface Sea Ice Melt in the CESM2 Improves Arctic Sea Ice Simulation
632 With Minimal Non-Polar Climate Impacts. *Journal of Advances in Modeling Earth Systems*
633 **14**, e2021MS002679 (2022).

- 634 63. DeRepentigny, P., Jahn, A., Holland, M. M. & Smith, A. Arctic Sea Ice in Two
635 Configurations of the CESM2 During the 20th and 21st Centuries. *Journal of Geophysical*
636 *Research: Oceans* **125**, e2020JC016133 (2020).
- 637 64. Yamagami, Y., Watanabe, M., Mori, M. & Ono, J. Barents-Kara sea-ice decline attributed to
638 surface warming in the Gulf Stream. *Nat Commun* **13**, 3767 (2022).
- 639 65. Guan, B. & Waliser, D. E. Detection of atmospheric rivers: Evaluation and application of an
640 algorithm for global studies. *J. Geophys. Res.* **120**, 12514–12535 (2015).
- 641 66. Rutz, J. J. *et al.* The Atmospheric River Tracking Method Intercomparison Project
642 (ARTMIP): Quantifying Uncertainties in Atmospheric River Climatology. *Journal of*
643 *Geophysical Research: Atmospheres* **124**, 13777–13802 (2019).
- 644 67. Lora, J. M., Shields, C. A. & Rutz, J. J. Consensus and Disagreement in Atmospheric River
645 Detection: ARTMIP Global Catalogues. *Geophysical Research Letters* **47**, e2020GL089302
646 (2020).
- 647 68. Zhang, P., Chen, G., Ma, W., Ming, Y. & Wu, Z. Robust Atmospheric River Response to
648 Global Warming in Idealized and Comprehensive Climate Models. *Journal of Climate* **34**,
649 7717–7734 (2021).
- 650 69. Swart, N. C., Fyfe, J. C., Gillett, N. & Marshall, G. J. Comparing Trends in the Southern
651 Annular Mode and Surface Westerly Jet. *Journal of Climate* **28**, 8840–8859 (2015).

652

653 **Acknowledgments**

654 We thank Jian Lu at PNNL, Sukyoung Lee and Steven B. Feldstein at PSU for helpful discussion.
655 We would like to acknowledge the CVCWG/NCAR for conducting the CESM2 simulations used
656 in this study and thank Adam Philips and Isla Simpson at NCAR for helpful information on these
657 model outputs. G.C. was supported by NSF Grants AGS-1832842 and NASA Grant
658 80NSSC21K1522. M.T. was funded by NASA award 80NSSC20K1254 and NSF award OPP-
659 1825858. L.R.L. was supported by the Office of Science, U.S. Department of Energy Biological
660 and Environmental Research as part of the Regional and Global Model Analysis program area.
661 B.G. was supported by NASA and the California Department of Water Resources.

662

663 **Author contributions**

664 P.Z. conceived the study, analyzed the data, and wrote the initial draft of the manuscript. G.C.,
665 M.T., and L.R.L. provided feedback on analysis and contributed to constructive revision. All
666 authors contributed to editing and revision.

667

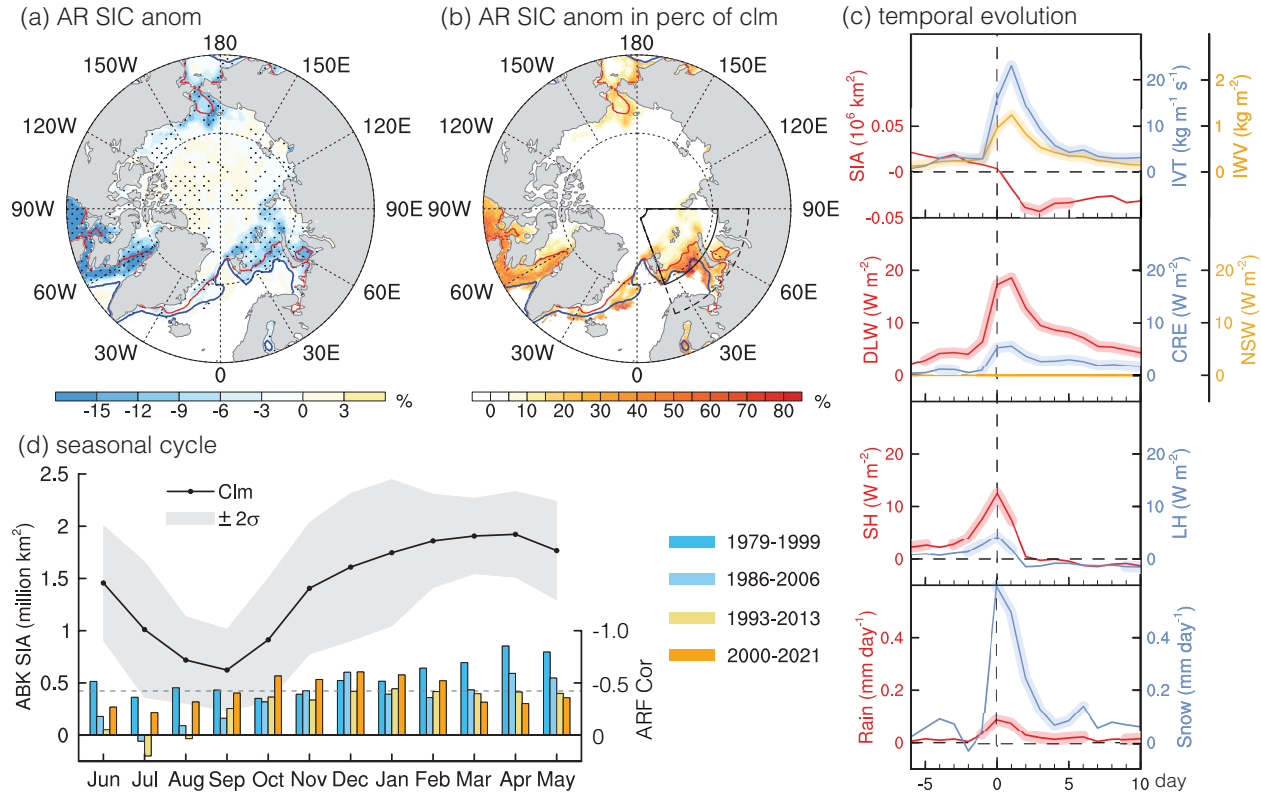
668 **Competing interests**

669 The authors declare no competing interests.

670

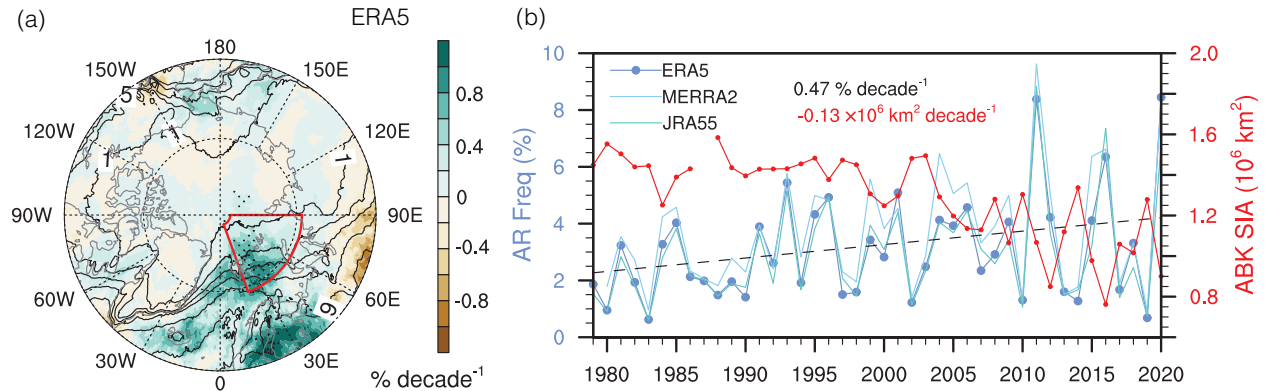
671 **Figure list:**

672

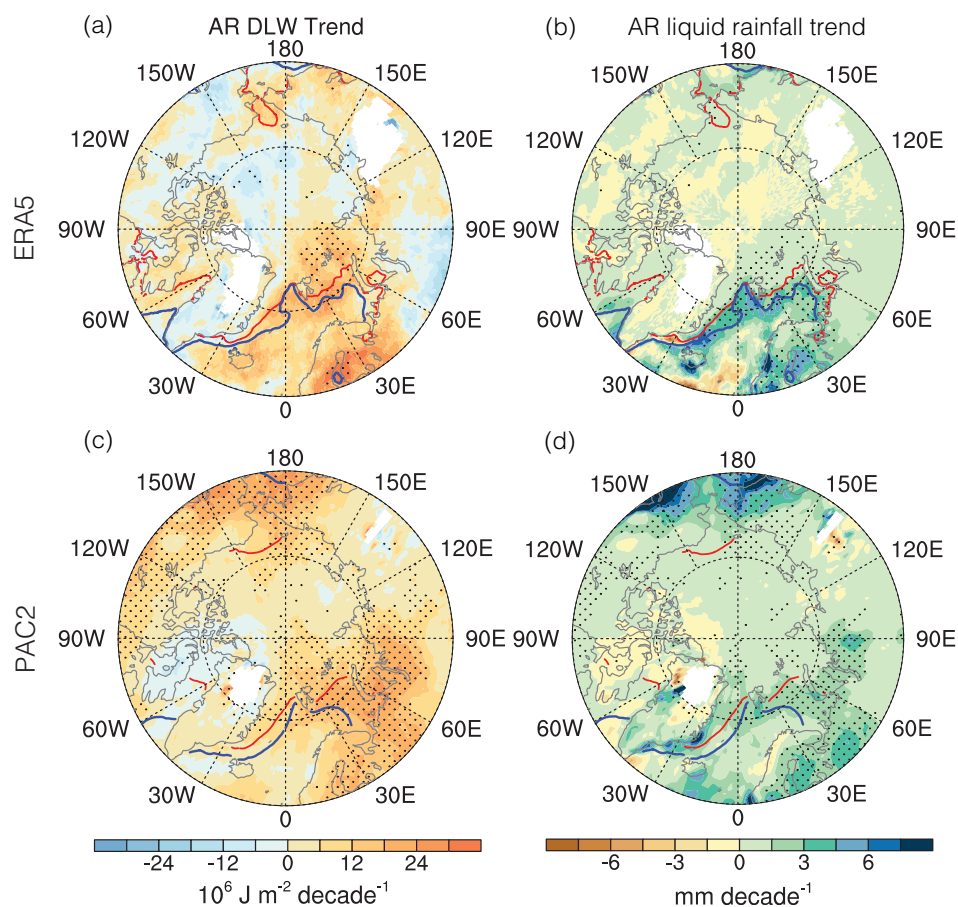


673
 674 **Fig. 1 Relationship between ARs and Arctic sea ice.** (a) NSIDC sea ice concentration (SIC,
 675 units: %) anomalies associated with ARs in November-December-January (NDJ) in 1979-2021
 676 (Methods). Red and blue lines are the climatological ice edges on Oct.31 and Jan.31, respectively,
 677 denoting the mean sea ice growth during NDJ. The region between these two ice edges is referred
 678 to as the marginal ice zone. (b) is the same as (a) but for the SIC anomalies in the percentage of
 679 climatology. The box (74°-88°N, 20°-90°E) highlights the Arctic-Barents-Kara (ABK) region. (c)
 680 Composite temporal evolution of the anomalies of the selected variables in ABK when ARs make
 681 “landfall” on the ice edge, including sea ice area (SIA), vertical integral of horizontal water vapor
 682 transport (IVT), vertical integral of water vapor (IWV), surface downward longwave radiation
 683 (DLW), cloud radiative effect (CRE) (the contribution of cloud to DLW), net surface shortwave
 684 radiation (NSW; almost zero), surface sensible heat flux (SH), surface latent heat flux (LH),
 685 rainfall, and snowfall. SIA is the total ice area in ABK calculated based on NSIDC SIC (Method),
 686 while other variables are area-averaged from ERA5 reanalysis data. Day-0 is the day of AR
 687 “landfalling” the ice cover (defined as at least one grid cell of an AR reaching the ice edge in
 688 ABK). The thick segments denote the anomalies are significant at the 95% confidence level. (d)
 689 Seasonal cycle of SIA over the ABK region and its correlation with AR frequency. Given the ice
 690 cover around ABK in winter may extend to the coast, we extend the southern boundary of the
 691 ABK area to 68°N (the dashed line in b) for the SIA calculation. Black line is the climatology in
 692 1979-2021 with an interval of 2 standard deviations (gray shading). The bars are the correlation
 693 coefficients between AR frequency and SIA in four overlapping 21-year segments (see legend) in
 694 1979-2021. The associated y-axis is on the right and inverted. Three-month running average is

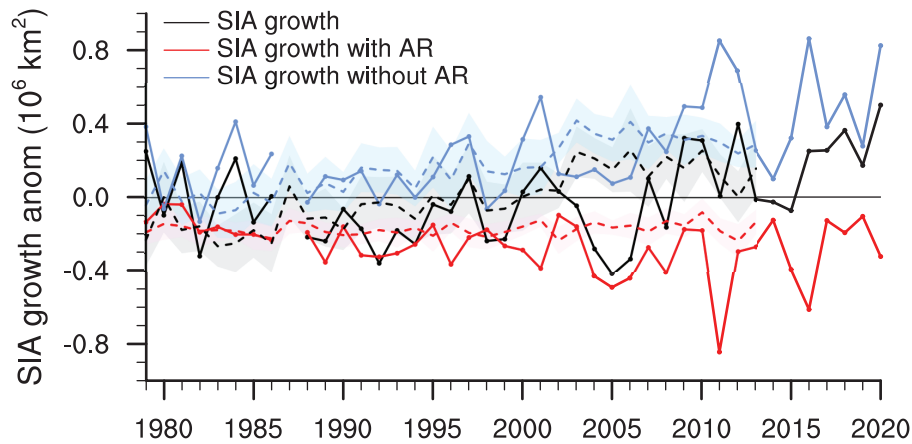
695 applied before the correlation calculation, i.e., the bars in Dec indicate the values of NDJ. The bars
 696 exceeding the dashed line denote the correlation is significant at the 95% confidence level.
 697
 698
 699



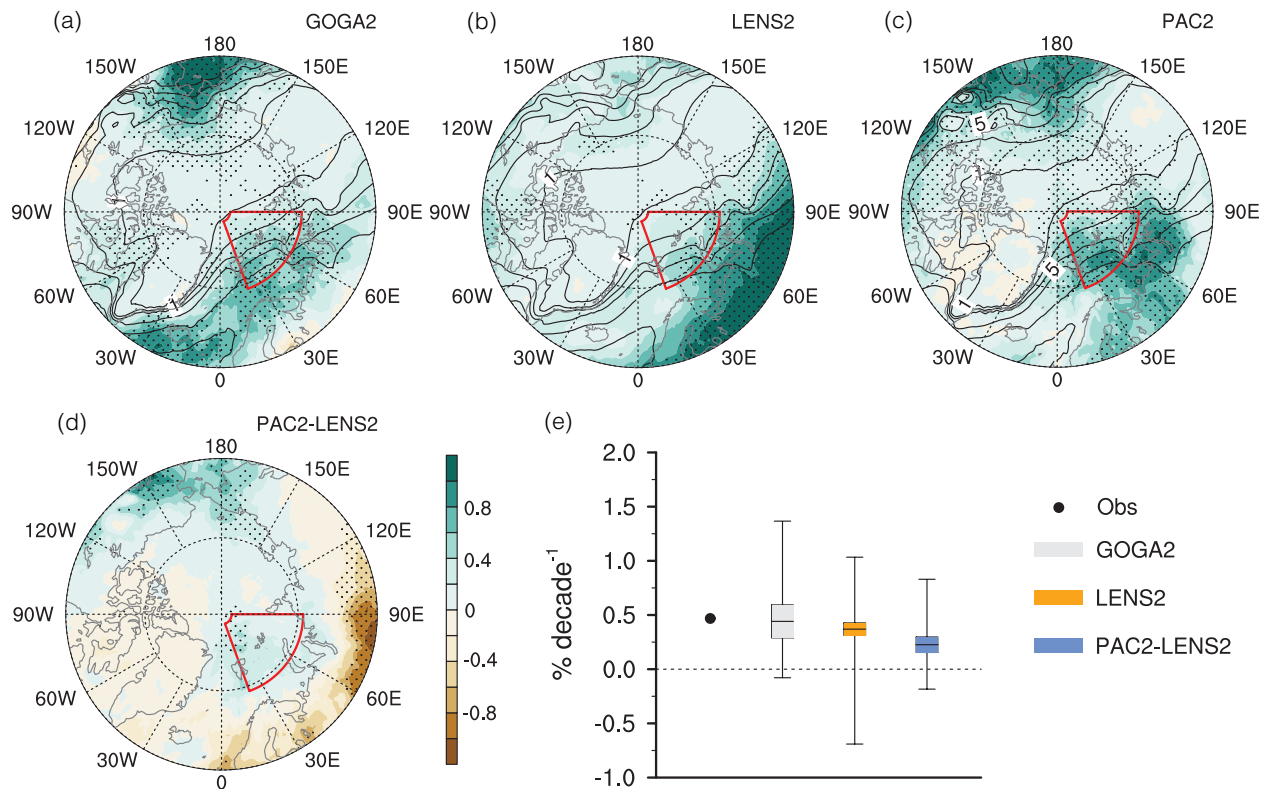
700
 701 **Fig. 2 Arctic AR frequency trends in recent decades.** (a) AR frequency trends (color shading)
 702 in NDJ in 1979-2021 from the ERA5 reanalysis. Contours are the climatology. (b) Area-averaged
 703 AR frequency time series in the ABK area (highlighted by the box in a) from three reanalysis
 704 datasets (ERA5, MERRA2, and JRA55). The dashed gray line is the linear trend of the ensemble
 705 mean of the three datasets. The red line is the time series of area sum SIA in ABK with missing
 706 data in the NDJ of 1987-88. Both the AR and SIA trends are significant at the 95% confidence
 707 level using *t*-test.
 708



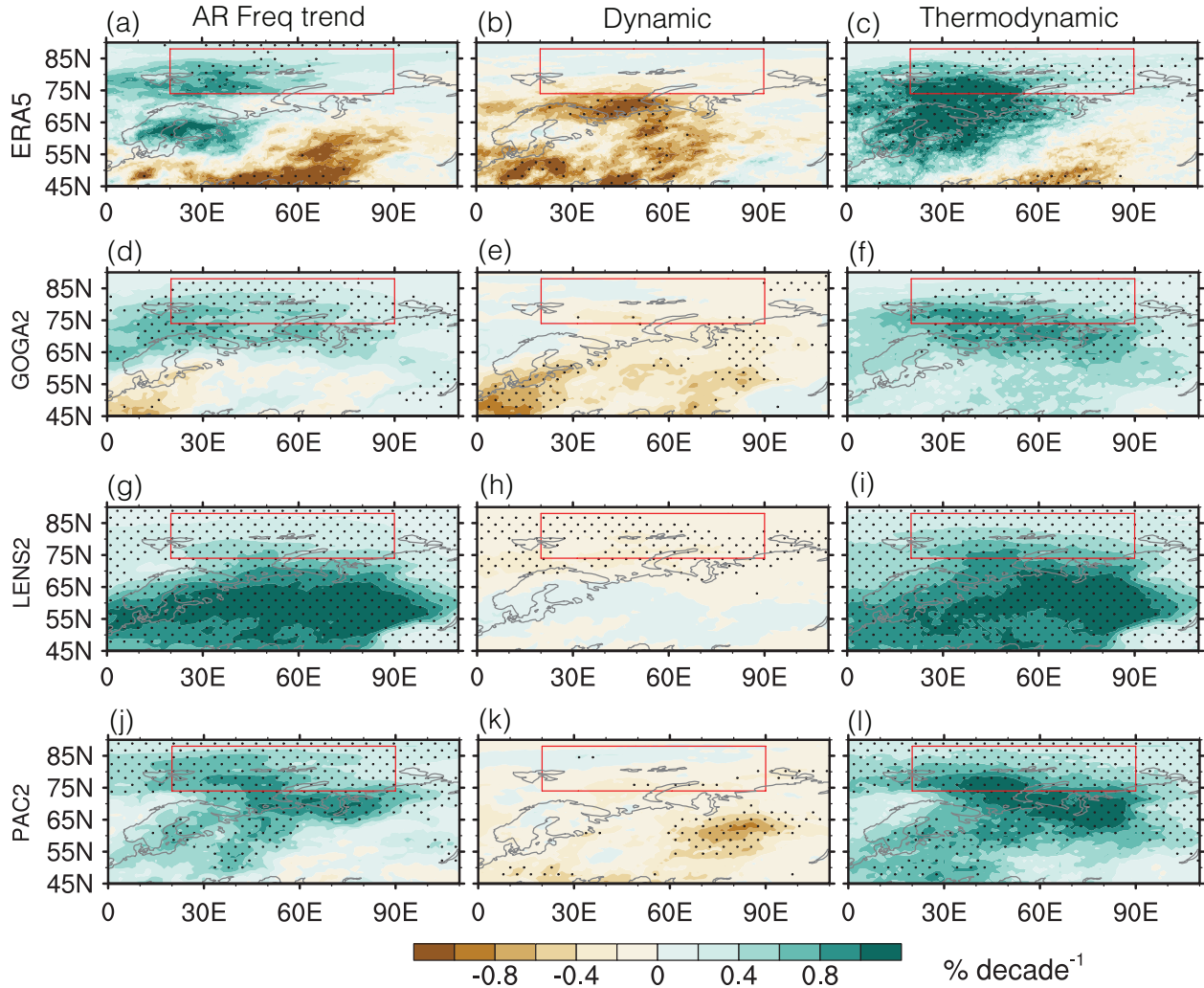
709
 710 **Fig. 3 Trends in the physical processes related to AR melting effect in recent decades.** Linear
 711 trends in cumulated DLW (a) and liquid rainfall (b) associated with ARs in NDJ in ERA5. See the
 712 calculation in Method. The AR-induced total DLW in ERA5 can be validated by the satellite
 713 observation CERES-SYN after 2000 (see Fig.S2). (c-d) the same as (a-b) but for the model
 714 ensemble from PAC2. Dots denote trends that are statistically significant at the 95% confidence
 715 level according to the *t*-test for ERA5 and the 1000-trail bootstrap resampling method for PAC2.
 716 Red and blue lines in (a-f) are the climatological sea ice cover edges on Oct.31 and Jan.31,
 717 respectively, denoting the mean sea ice growth in NDJ.
 718



719
 720 Fig. 4 **Sea ice area growth in early winter.** SIA growth is the cumulative sum of the daily
 721 anomalies of SIA day-to-day tendency in NDJ (Method). The solid lines denote the total SIA
 722 growth in the whole season (black), SIA growth associated with the ARs (red), SIA growth without
 723 the effects of ARs (light blue) in observation. The SIA growth associated with ARs denotes the
 724 melting effect of ARs on ABK SIA in NDJ. The negative trends of melting effect (red) and the
 725 positive trend in SIA growth without the impact of ARs (light blue) are significant at $P < 0.01$, while
 726 the trend in whole season SIA growth (black) is less significant. The dashed lines show the SIA
 727 growth in PAC2 with standard error (color shading). The trend in melting effect in PAC2 is less
 728 significant, although PAC2 well reproduces the observed AR frequency change (see Fig.5). This
 729 may be attributable to the model bias in CESM2 sea ice simulations (see Method).
 730



731
 732 **Fig. 5 AR frequency trends in NDJ in model ensembles.** (a-c) Same as Fig.2(a) but for the
 733 GOGA2, LENS2, PAC2 ensembles. Agreements for the sign of AR changes among members of
 734 each ensemble are shown in Fig.S7. (d) AR changes due to tropical Pacific variability calculated
 735 as the difference between the ensemble means of PAC2 and LENS2 (see Model experiments and
 736 interpretation in Method). Dots denote trends that are statistically significant at 95% confidence
 737 level according to 1000-trail bootstrap resampling method in (a-d). (e) Uncertainties of area-
 738 averaged AR trends in each model ensemble. The horizontal lines inside the color bars represent
 739 the ensemble mean. The color bars show the 95% confidence interval (Method). The upper and
 740 lower whiskers denote the 5th and 95th percentiles of the trends across the ensemble (i.e., the
 741 minimum and maximum for GOGA2 and PAC2, 3rd minimum and maximum for LENS2). The
 742 blue bar is calculated based on the 10 members in PAC2 by removing the ensemble mean of
 743 LENS2, denoting the uncertainty of the contribution of tropical Pacific variability. The black dot
 744 shows the mean of the three reanalysis datasets, representing the observation. The LENS2 trend
 745 has a narrower confidence interval due to its larger ensemble size.
 746



747

748

749

750

751

752

753

754

755

Fig. 6 **Mechanisms of the AR changes.** NDJ AR frequency trend in ERA5 (a), which is reproduced from Fig.2(a) but shown in cylindrical map projection here. Contributions of dynamic and thermodynamic effects to the AR trend (b-c). (d-l) are similar to (a-c) but for GOGA2 (d-f), LENS2 (g-i), and PAC2 (j-l). Similarly, (d, g, j) are reproduced from Fig.5 (a, b, c) but shown in cylindrical map projection, respectively. Dots denote that the variables are statistically significant at the 95% confidence level according to the *t*-test for (a-c) and 1000-trail bootstrap resampling methods for (d-l), respectively. The red box in each subplot delineates the ABK region.

19 Calculation of IVT

20 Reanalysis datasets: The daily wind and specific humidity at standard pressure levels below
 21 200hPa are used to calculate the vertical integral of water vapor transport (IVT) for AR detection
 22 (Eq. 1). The integral of water vapor (IWW) is also calculated (Eq. 2).

$$23 \quad \overrightarrow{IVT} = -\frac{1}{g} \int_{sfc}^{200hPa} \overrightarrow{V} q dp = -\frac{1}{g} \left(\int_{sfc}^{200hPa} u q dp + \int_{sfc}^{200hPa} v q dp \right) \quad (1)$$

$$24 \quad \overrightarrow{IWW} = -\frac{1}{g} \int_{sfc}^{200hPa} q dp \quad (2)$$

25 Where g is the gravitational acceleration (m s^{-2}), q is the specific humidity (kg kg^{-1}), \overrightarrow{V} is the wind
 26 vector (m s^{-1}) composed by zonal wind (u) and meridional wind (v), and p is the atmospheric
 27 pressure (hPa).

28 Model outputs: Due to the data availability, only the daily wind and specific humidity at the surface
 29 level, 850, 500, 200hPa are used in GOGA2 and PAC2. For LENS2, variables at the surface level,
 30 850, 700, 500, 200hPa are available. There is almost no difference in the IVT calculation with or
 31 without the data at 700hPa, especially in the view of anomaly or trend. Thus, including 700hPa
 32 data in LENS2 does not impact the comparison between the ensembles in the view of the trend.
 33 At the grid where the bottom level is higher than 850hPa (and/or 700hPa for LENS2), i.e. the
 34 mountain regions, the values at the 850hPa (and/or 700hPa for LENS2) are excluded.

35

36 Sensitivity to the choice of AR detection threshold

37 In the polar regions, the choice of the AR detection threshold is region-dependent. For example,
 38 98th percentile and $50 \text{ kg m}^{-1} \text{ s}^{-1}$ are used in different regions of the Antarctic (Wille et al. 2019;
 39 Francis et al. 2020), while the $150 \text{ kg m}^{-1} \text{ s}^{-1}$ criterion is used in southern Greenland (Mattingly et
 40 al. 2018). In most regions of the Arctic, the absolute IVT threshold of $100 \text{ kg m}^{-1} \text{ s}^{-1}$ used in the
 41 current study is about 87-99th percentile in NDJ (FigS.3), indicating the IVT of a relative threshold
 42 varies largely in a relatively small region. We also checked the AR detection with relative
 43 thresholds, such as 90th, 95th, and even 98th percentile, shown in (FigS.1 d-f). In all three cases,
 44 the trend of AR frequency in the region of interest is significant and qualitatively consistent with
 45 that with the absolute threshold of $100 \text{ kg m}^{-1} \text{ s}^{-1}$. Furthermore, using the original thresholds (85th
 46 percentile or $100 \text{ kg m}^{-1} \text{ s}^{-1}$, whichever is greater) facilitates the discussion of the spatial pattern of
 47 AR changes involving the midlatitudes. Thus, we keep the 85th percentile or $100 \text{ kg m}^{-1} \text{ s}^{-1}$ for AR
 48 detection in this study.

49

50 Comparison between ARs, extreme transient transport, and moisture intrusion for the total 51 Arctic moisture import

52 Previous studies have shown that the variability of the Arctic water vapor is driven by moisture
 53 transport, which is dominated by transient weather systems (89-94% at 70°N) (Rinke et al. 2009;
 54 Dufour et al. 2016), including moisture intrusion (Woods et al. 2013), extreme transient transport
 55 (Liu and Barnes 2015), and ARs (Nash et al. 2018). These weather systems including warm
 56 conveyor belts have overlapping features but by no means identical concepts of atmospheric flow

57 (Sodemann et al. 2020). The moisture intrusions, defined by using the vertical integral of
58 meridional moisture transport ($\int v'q'$), the meridional component of Eq. 1, with a threshold of 200
59 $\text{Tg d}^{-1} \text{ deg}^{-1}$ ($\sim 90^{\text{th}}$ percentile), account for 36% of the total poleward moisture transport across
60 70°N in winter (Woods et al. 2013). The extreme meridional transients ($v'q'$, where the prime
61 denotes the deviation from the climatological mean) defined with a threshold of 90^{th} percentile
62 account for 38% of the total poleward transport across 70°N in winter and 32% in summer (Liu
63 and Barnes 2015). In contrast, the ARs, usually identified using IVT (the complete form of Eq. 1),
64 account for 70-80% of the total poleward moisture transport across 70°N (Nash et al. 2018). Here
65 we confirm the climatological fractions at a range of high latitude-Arctic circles using ERA5 daily
66 data as shown in Table S1. Although the values decrease along with the latitudes due to the low
67 temperature, ARs still dominate the Arctic moisture import. The distinct portions of poleward
68 moisture transports explained by moisture intrusion, extreme meridional transients, and ARs lie in
69 their definitions. The moisture intrusion and extreme meridional transients are defined based on
70 only the meridional component of IVT with a threshold of 90^{th} percentile, and thus they preclude
71 the strong poleward moisture transport with a relatively weak meridional component but a strong
72 zonal component, i.e., the poleward moisture transport events tilting zonally. In fact, the latter is
73 more common in mid-high latitude due to the prevailing westerly wind. Including all kinds of
74 strong moisture transports, the median direction of ARs is $\sim 60^{\circ}$ in North Hemisphere and $\sim 120^{\circ}$
75 in South Hemisphere (0° = northward; 90° = eastward) (Guan and Waliser 2015), which is to say
76 the strong poleward moisture transport events are more zonal than meridional. Given AR's
77 definition is more representative of strong poleward moisture transport events, ARs could be
78 regarded as the major weather system that drives the Arctic moisture imports (70-80% at 70°N ,
79 Nash et al. 2018), and therefore be used to explore the moisture-induced melting effect on the
80 Arctic sea ice.

81

82 **Quality and validation of reanalysis datasets**

83 Despite the biases in magnitude, the spatial and temporal patterns of Arctic moisture transport in
84 the reanalysis datasets show a remarkable agreement with the radiosondes (Dufour et al. 2016).
85 Surface downward longwave radiation flux (DLW) in ERA5 is validated using satellite-derived
86 data, Synoptic TOA and surface fluxes and clouds (SYN) version 4 from the Clouds and the
87 Earth's Radiant Energy System (CERES) project (Doelling et al. 2016). CERES-SYN is available
88 at a daily time scale at a $1^{\circ} \times 1^{\circ}$ resolution from March 2000 to the present. CERES-SYN is
89 available from <https://ceres.larc.nasa.gov/data/>. Fig. S2 shows that the DLW in ERA5 agrees well
90 with the satellite data, especially during the AR events in NDJ, suggesting the results related to
91 DLW are reliable. Similar to radiation, rainfall and snowfall in ERA5 are also derived from the
92 assimilation system of reanalysis. There is no long-period observation over the wide ocean for
93 these two variables and thus they are hard to be validated. Generally, their reliability is relatively
94 lower than commonly used variables, such as temperature, wind, et al, from the same reanalysis
95 dataset. That is to say, the results related to rainfall could have unknown uncertainty, although
96 intrinsic dynamical consistency exists among all variables in each reanalysis dataset.

97

98 **Ice drift related to ARs**

99 We estimate the anomalous SIA due to AR wind-induced ice drifting in ABK in NDJ based on
 100 NSIDC Polar Pathfinder Daily 25 km EASE-Grid Sea Ice Motion Vectors dataset (Tschudi et al.
 101 2019), which is available from <https://nsidc.org/data/NSIDC-0116>. AR wind-induced ice drift in
 102 ABK is defined as the net ice drift across the ABK boundary when an AR is approaching or
 103 crossing the ice cover in ABK. The cumulated ice drift anomalies in NDJ associated with AR wind
 104 are smaller by 2-3 orders of magnitude compared to the AR-related SIA anomaly. The strong wind
 105 could change the ice distribution around the wind flow, such as SIC redistribution within a cyclone
 106 (Clancy et al. 2022), but change little the total SIA in a much larger region such as ABK. Thus,
 107 the big picture of ARs' impact on sea ice coverage lies in thermodynamic ice melting.

108

109 References for Supplementary Information:

110 Clancy, R., C. M. Bitz, E. Blanchard-Wrigglesworth, M. C. McGraw, and S. M. Cavallo, 2022: A
 111 cyclone-centered perspective on the drivers of asymmetric patterns in the atmosphere and
 112 sea ice during Arctic cyclones. *Journal of Climate*, **35**, 73–89,
 113 <https://doi.org/10.1175/JCLI-D-21-0093.1>.

114 Doelling, D. R., M. Sun, L. T. Nguyen, M. L. Nordeen, C. O. Haney, D. F. Keyes, and P. E.
 115 Mlynchak, 2016: Advances in Geostationary-Derived Longwave Fluxes for the CERES
 116 Synoptic (SYN1deg) Product. *Journal of Atmospheric and Oceanic Technology*, **33**, 503–
 117 521, <https://doi.org/10.1175/JTECH-D-15-0147.1>.

118 Dufour, A., O. Zolina, and S. K. Gulev, 2016: Atmospheric Moisture Transport to the Arctic:
 119 Assessment of Reanalyses and Analysis of Transport Components. *Journal of Climate*, **29**,
 120 5061–5081, <https://doi.org/10.1175/JCLI-D-15-0559.1>.

121 Francis, D., K. S. Mattingly, M. Temimi, R. Massom, and P. Heil, 2020: On the crucial role of
 122 atmospheric rivers in the two major Weddell Polynya events in 1973 and 2017 in
 123 Antarctica. *Science Advances*, **6**, eabc2695, <https://doi.org/10.1126/sciadv.abc2695>.

124 Guan, B., and D. E. Waliser, 2015: Detection of atmospheric rivers: Evaluation and application of
 125 an algorithm for global studies. *J. Geophys. Res.*, **120**, 12514–12535,
 126 <https://doi.org/10.1002/2015jd024257>.

127 Liu, C., and E. A. Barnes, 2015: Extreme moisture transport into the Arctic linked to Rossby wave
 128 breaking. *J. Geophys. Res.*, **120**, 2014JD022796, <https://doi.org/10.1002/2014JD022796>.

129 Mattingly, K. S., T. L. Mote, and X. Fettweis, 2018: Atmospheric River Impacts on Greenland Ice
 130 Sheet Surface Mass Balance. *Journal of Geophysical Research: Atmospheres*, **123**, 8538–
 131 8560, <https://doi.org/10.1029/2018JD028714>.

132 Nash, D., D. Waliser, B. Guan, H. Ye, and F. M. Ralph, 2018: The Role of Atmospheric Rivers in
 133 Extratropical and Polar Hydroclimate. *Journal of Geophysical Research: Atmospheres*,
 134 **123**, 6804–6821, <https://doi.org/10.1029/2017JD028130>.

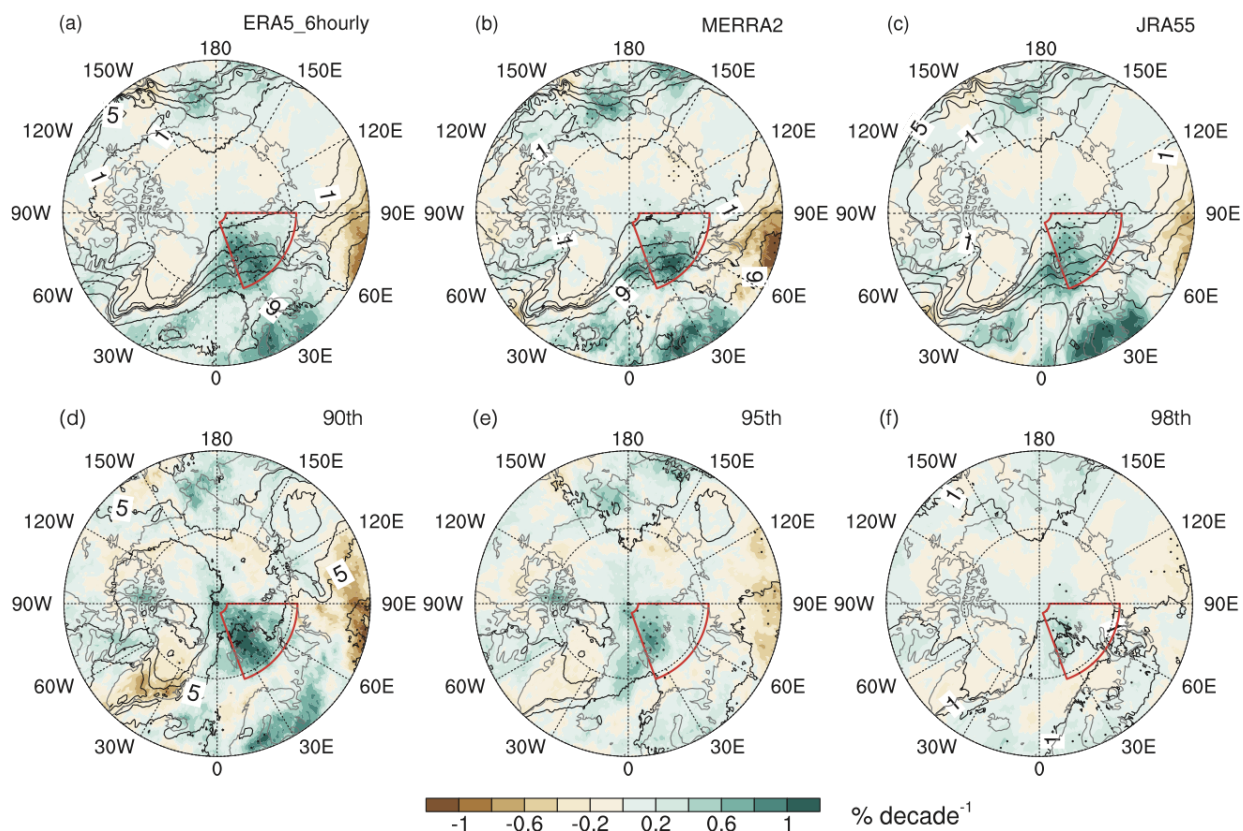
135 Rinke, A., C. Melsheimer, K. Dethloff, and G. Heygster, 2009: Arctic Total Water Vapor:
 136 Comparison of Regional Climate Simulations with Observations, and Simulated Decadal

- 137 Trends. *Journal of Hydrometeorology*, **10**, 113–129,
138 <https://doi.org/10.1175/2008JHM970.1>.
- 139 Sodemann, H., and Coauthors, 2020: Structure, Process, and Mechanism. *Atmospheric Rivers*,
140 Springer, p. 252.
- 141 Tschudi, M., W. N. Meier, J. S. Stewart, C. Fowler, and J. Maslanik, 2019: *Polar Pathfinder Daily*
142 *25 km EASE-Grid Sea Ice Motion Vectors, Version 4*. NASA National Snow and Ice Data
143 Center Distributed Active Archive Center, <https://doi.org/10.5067/INAWUWO7QH7B>.
- 144 Wille, J. D., V. Favier, A. Dufour, I. V. Gorodetskaya, J. Turner, C. Agosta, and F. Codron, 2019:
145 West Antarctic surface melt triggered by atmospheric rivers. *Nature Geoscience*, **12**, 911–
146 916, <https://doi.org/10.1038/s41561-019-0460-1>.
- 147 Woods, C., R. Caballero, and G. Svensson, 2013: Large-scale circulation associated with moisture
148 intrusions into the Arctic during winter. *Geophysical Research Letters*, **40**, 4717–4721,
149 <https://doi.org/10.1002/grl.50912>.
- 150

151 **Supplementary Figures**

152

153



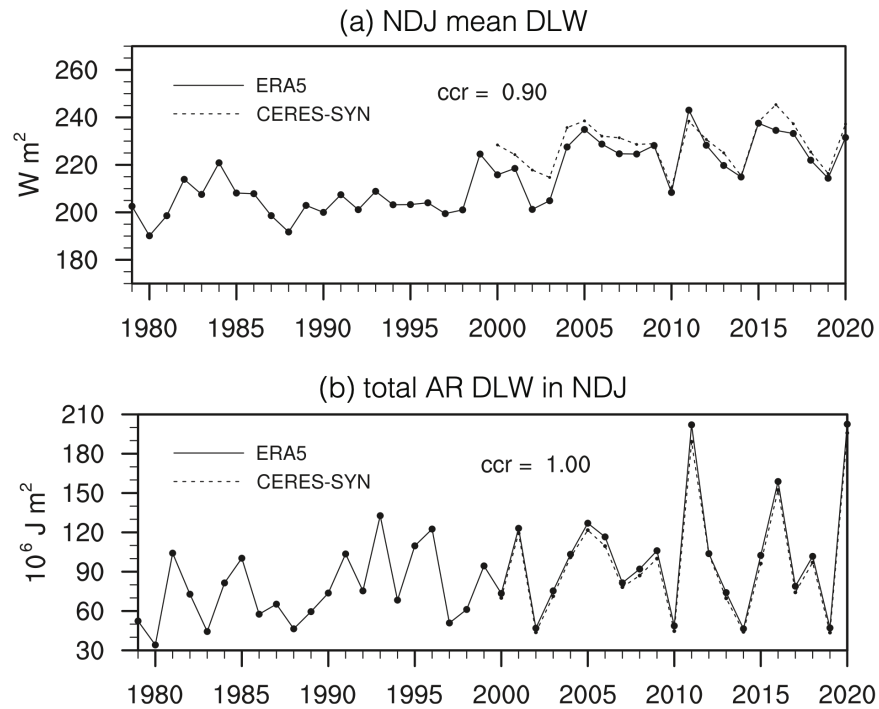
154

155 Fig.S1 Observed AR frequency trend similar to Fig. 2a but with ERA5 6 hourly data (a), MERRA2

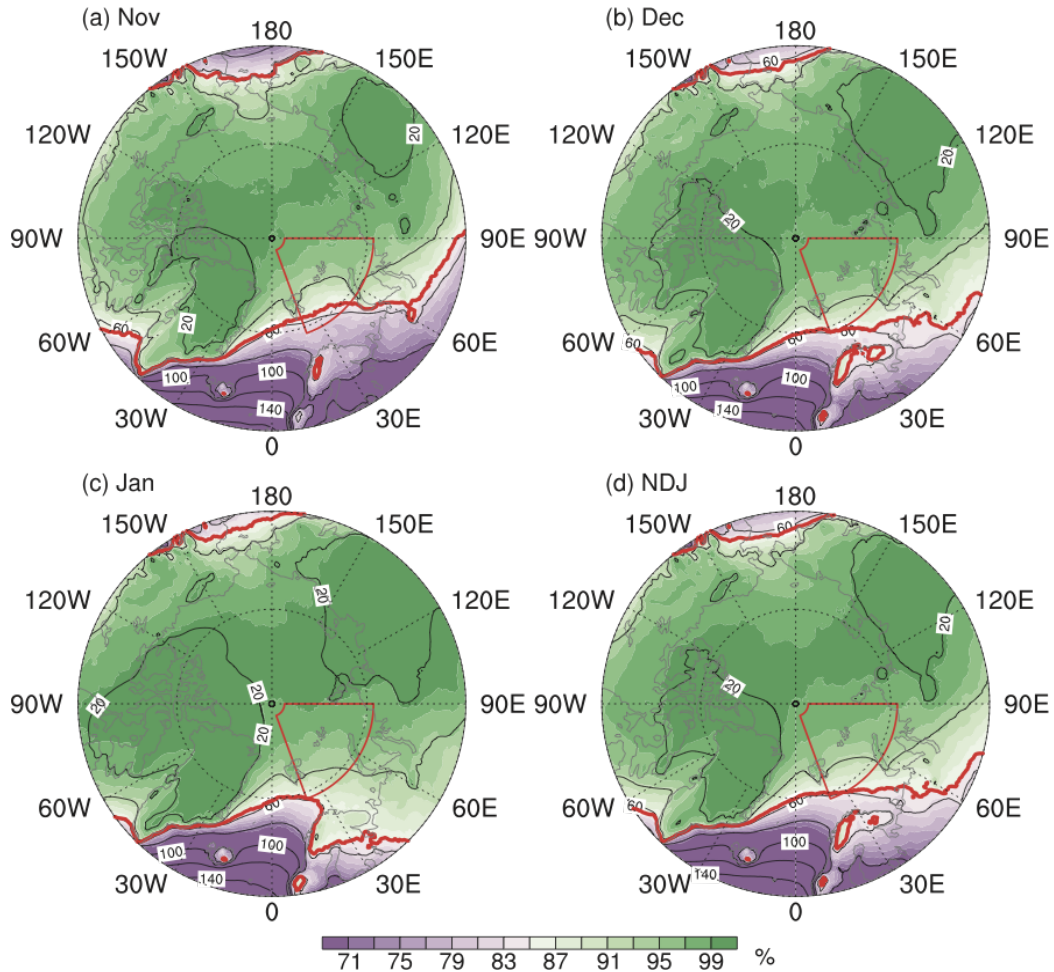
156 daily data (b), JRA55 daily data (c). (d-f) same as Fig2.a but the ARs are detected using 90th (d),

157 95th (e), and 98th (f) percentile. The red box in each panel highlights the region of interest.

158

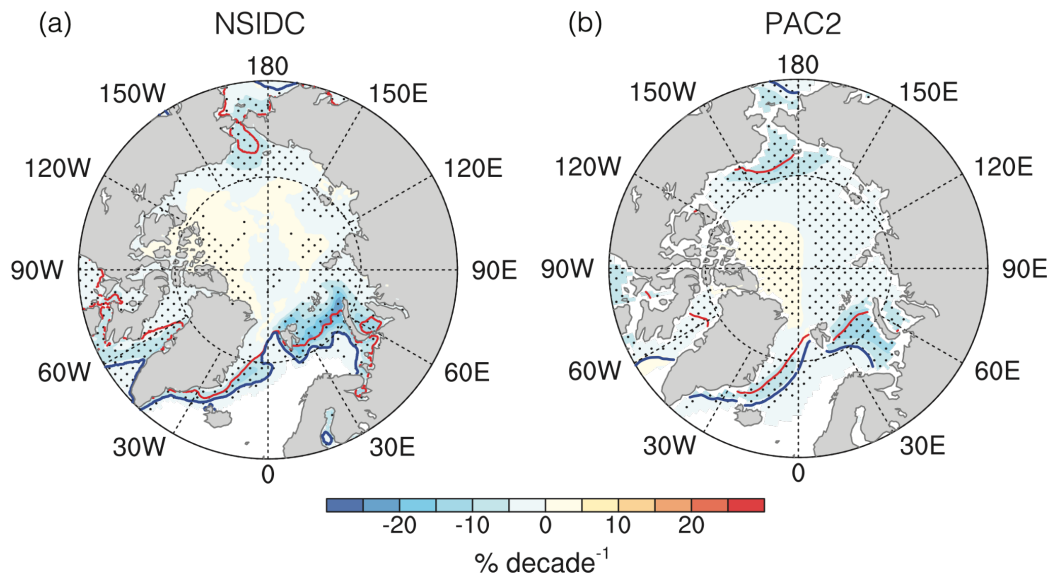


159
 160 Fig.S2 Validation of downward longwave radiation at the surface (DLW) in ERA5. (a) Time series
 161 of NDJ mean DLW (W m^{-2}) in ABK area in reanalysis dataset ERA5 in 1979-2020 (solid) and
 162 satellite observation CERES-SYN (dashed) in 2000-2020. The digits denote the correlation
 163 coefficient between these two time series during the period of 2000-2020. (b) Same as (a) but for
 164 AR-induced total longwave radiation (10^6 J m^{-2}) in NDJ. Note that the values in (b) are the results
 165 of integration over time (Method), and thus the units are different in these two panels. The DLW
 166 in ERA5 has a remarkable agreement with satellite observation, especially during the AR activities.
 167



168
 169
 170
 171
 172

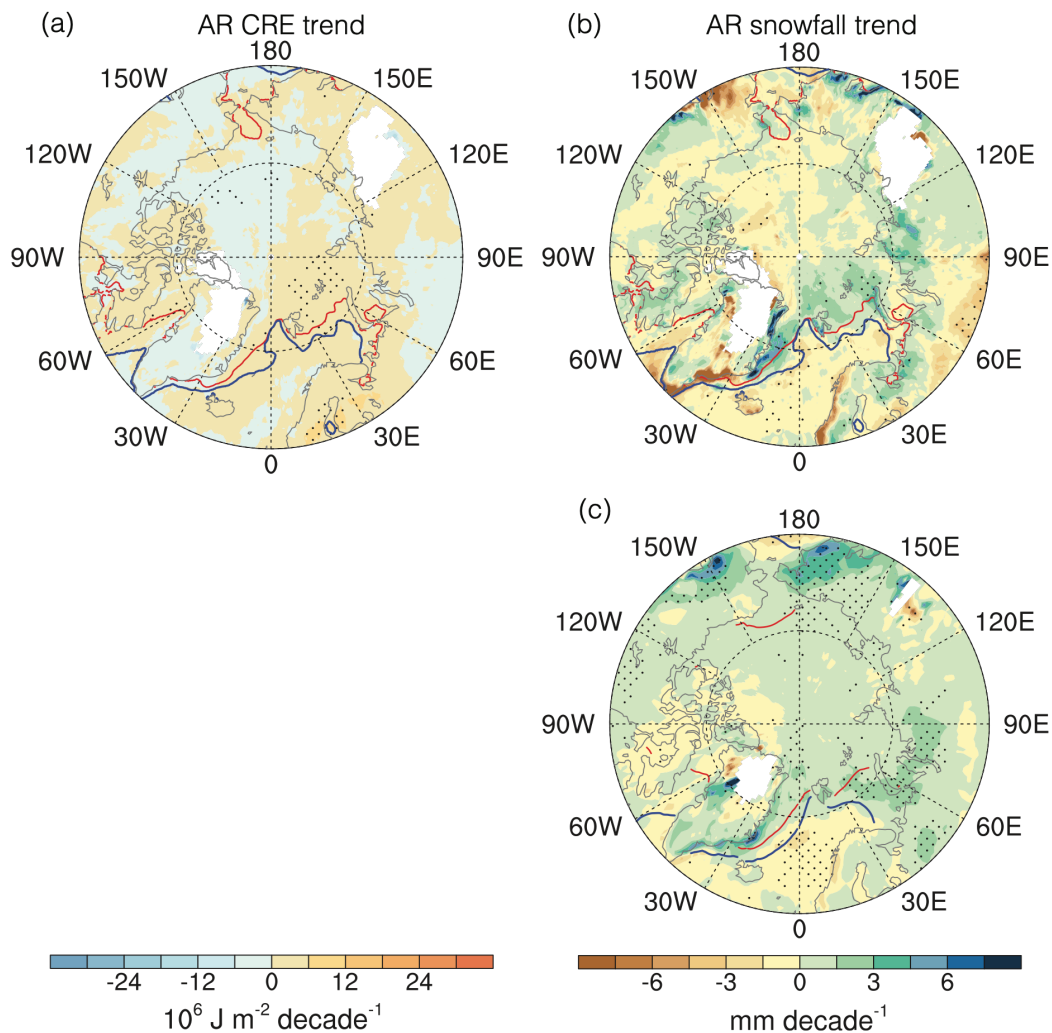
Fig.S3 Percentile of $100 \text{ kg m}^{-1} \text{ s}^{-1}$ IVT in Nov, Dec, Jan, and whole NDJ. Black contours show the climatology of IVT. The red thick line in each subplot highlights the 85th percentile contour of $100 \text{ kg m}^{-1} \text{ s}^{-1}$ IVT.



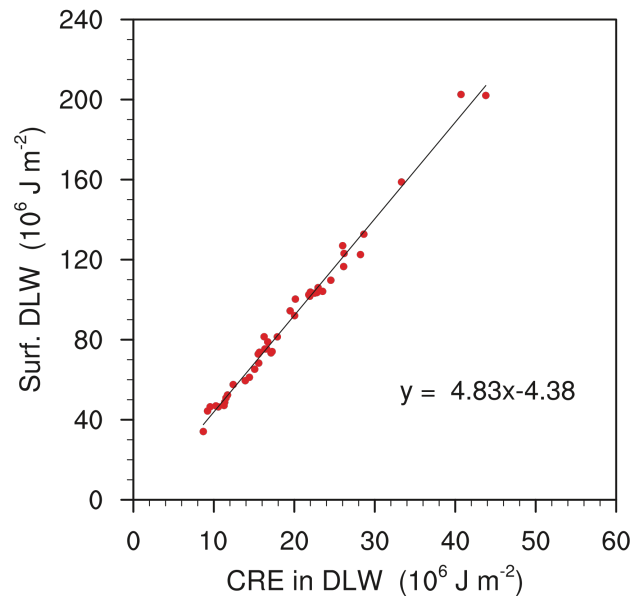
173

174 Fig.S4 Trends in sea ice concentration (SIC) in NDJ in recent decades. (a) Trend in 1979-2020 in
175 NSIDC. (b) Trend in 1979-2013 in the model ensemble from PAC2. Unit is % decade⁻¹.

176

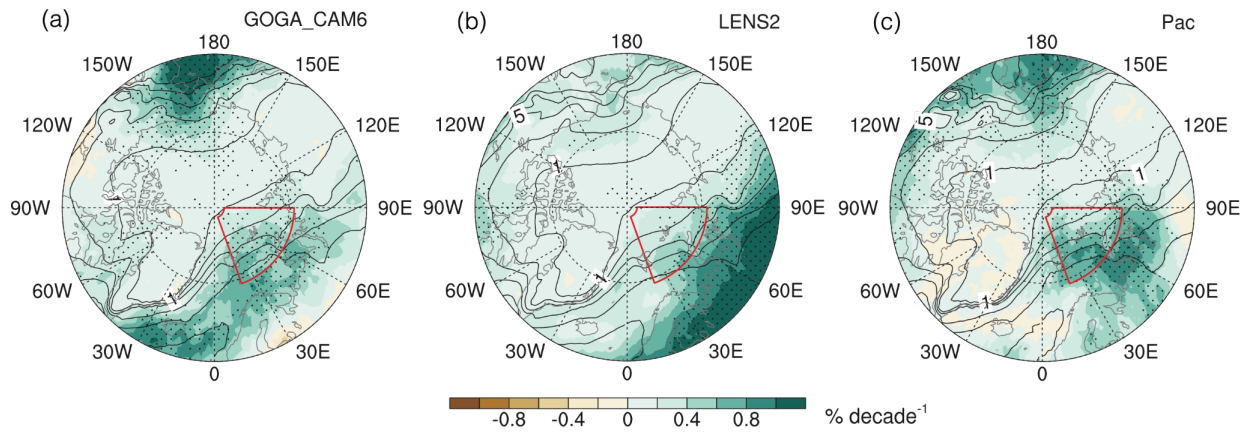


177
 178 Fig.S5 AR-induced trends in cloud radiative effect in cumulated DLW (left) and snowfall (right)
 179 in NDJ in ERA5 (a,b) and the model ensemble from PAC2 (c). See Method for the calculation
 180 details of the total amounts of the flux variables associated with ARs in NDJ. The cloud radiative
 181 effect of DLW is expressed as the difference between DLW and clear sky DLW. The cloud
 182 radiative effect of longwave radiation in PAC2 is missing due to no clear sky DLW output in PAC2.
 183



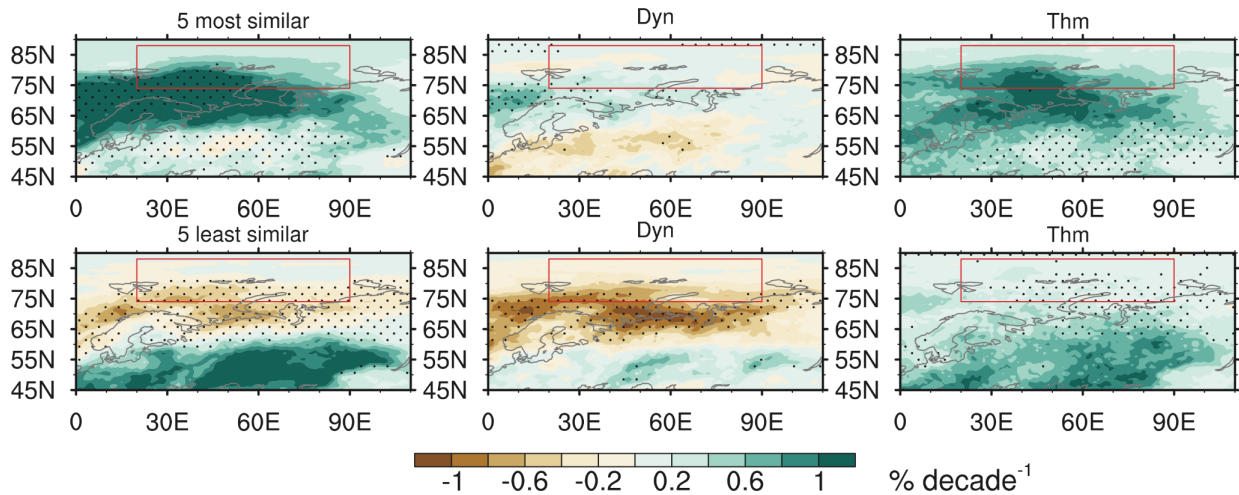
184
185
186
187

Fig.S6 Proportional contribution of cloud radiative effect to the cumulated surface DLW related to ARs in NDJ in 1979-2020 in ERA5. The linear fit is shown as the black line and the equation.



188
189
190
191

Fig.S7 Agreement for the sign of the AR changes among members in each ensemble. (a-c) the same as Fig.5(a-c) but the dots denote >80% agreement among ensemble members.



192
 193
 194
 195
 196
 197
 198
 199
 200
 201
 202

Fig.S8 AR frequency trend in selected individual members in LENS2. The left column shows the mean AR frequency trend in 5 LENS2 members who are most (least) similar to GOGA2 in the area of (0°-110°E, 45°-90°N). Here, we regard the AR trend pattern in GOGA2 as the reference pattern considering the system consistency. The results are similar for using PAC2 as the reference pattern. The middle and right columns are the contributions of dynamic and thermodynamic effects, similar to that in Fig.6. The dots indicate the AR changes are significantly different from the other 45 members in LENS2 using the 1000 times bootstrap resampling methods. The results are similar in the composites of the LENS2 sub-ensembles with the largest (smallest) trends in ABK, which we have confirmed.

203 **Supplementary tables**

204

205 **Table S1 Fraction of mean annual total poleward IVT explained by ARs in ERA5 in 1979-2021**

<i>60°N</i>	<i>65°N</i>	<i>70°N</i>	<i>75°N</i>	<i>80°N</i>
81%	78%	75%	71%	69%

206